Chemical Engineering Journal 500 (2024) 156900

Contents lists available at ScienceDirect

Chemical Engineering Journal

journal homepage: www.elsevier.com/locate/cej

Integration of a 3D-printed electrochemical reactor with a tubular membrane photoreactor to promote sulfate-based advanced oxidation processes

Agustina R. de Olivera [a,b,c,1], Carla S. Santos [a,b,1], Ismael F. Mena [c], Miguel A. Montiel [c], Rosa Montes [d], José B. Quintana [d], Rosario Rodil [d], Ana I. Gomes [a,b], Francisca C. Moreira [a,b], Jan Gäbler [e], Lothar Schäfer [e], C. Sáez [c], Manuel A. Rodrigo [c,*], Vítor J.P. Vilar [a,b,*]

[a] LSRE-LCM – Laboratory of Separation and Reaction Engineering – Laboratory of Catalysis and Materials, Faculty of Engineering, University of Porto, Rua Dr. Roberto Frias, 4200-465 Porto, Portugal
[b] ALiCE – Associate Laboratory in Chemical Engineering, Faculty of Engineering, University of Porto, Rua Dr. Roberto Frias, 4200-465 Porto, Portugal
[c] Department of Chemical Engineering. Faculty of Chemical Sciences & Technologies. University of Castilla-La Mancha, Campus Universitario s/n, 13071 Ciudad Real, Spain
[d] Aquatic One Health Research Center (iARCUS) & Department of Analytical Chemistry, Nutrition and Food Chemistry. R. Constantino Candeira S/N, IIAA building, Universidade de Santiago de Compostela, 15782 Santiago de Compostela, Spain
[e] Fraunhofer Institute for Surface Engineering and Thin Films IST, 38108 Braunschweig, Germany

ARTICLE INFO

Keywords:
Peroxomonosulfate
Peroxydisulfate
Electrogeneration
Membrane concentrates
Contaminants of emerging concern

ABSTRACT

This study investigates the integration of an in-house 3D printed electrochemical cell – SERPIC-UCLM® cell – for the in situ generation of peroxymonosulfuric acid (PMSA) with a lab-scale tubular membrane photoreactor (TMPr) to evaluate the effectiveness of sulfate-radical advanced oxidation processes (SR-AOPs) in eliminating contaminants of emerging concern (CECs) from reverse osmosis and nanofiltration concentrates (RO_C and NF_C, respectively). First, the SERPIC-UCLM® cell was evaluated in terms of mass transport features employing the limiting current technique, demonstrating favorable volumetric mass transport rates ($k_mA \sim 10^{-3}$ s^{-1}) and Sherwood values ($Sh > 300$) under the laminar flow regime ($110 <$ Reynolds (Re) < 790). Afterward, the effect of the electrolyte (sulfuric acid, H_2SO_4) initial pH in the electrochemical generation of PMSA was studied, with an initial pH of 1 selected as optimal. PMSA is a highly reactive peroxyacid that undergoes self-decomposition at neutral pH media (e.g., RO_C and NF_C with a pH of 7.6 and 7.9, respectively), primarily existing in the form of peroxomonosulfate (PMS). Additionally, the phototreatment of the RO_C and NF_C was assessed using the electrogenerated PMS and commercial peroxydisulfate (PDS) under the same conditions. The results indicated comparable degradation patterns for CECs in both RO_C and NF_C. Furthermore, the application of 2.4 mM PMS resulted in removals higher than 60 % for 7 of the 11 CECs identified in the NF_C, and ensured compliance with wastewater discharge regulations for pH, chemical oxygen demand (COD), and total suspended solids (TSS) levels. These findings emphasize the importance of this technology, showing its advantages in terms of versatility and logistics.

1. Introduction

Wastewater reuse represents a promising solution to water scarcity problems in various fields of application, particularly in the agricultural sector, for which water supply accounts for more than 70 % of demand [1]. However, conventional treatment technologies usually employed in wastewater treatment plants (WWTPs) are ineffective in the removal of a significant portion of pollutants, namely the collectively known contaminants of emerging concern (CECs) [2]. These CECs include antibiotics, drugs, natural and synthetic hormones, resistant bacteria and viruses, and other refractory chemicals from the industry [3,4]. Although the European Union has invested in research and established

* Corresponding authors at: Tel.: +34 639621112 (Manuel A. Rodrigo); Tel.: +351 918257824 (Vítor J.P. Vilar).
E-mail addresses: Manuel.Rodrigo@uclm.es (M.A. Rodrigo), vilar@fe.up.pt (V.J.P. Vilar).
[1] The first two authors contributed equally to this work.

https://doi.org/10.1016/j.cej.2024.156900
Received 12 July 2024; Received in revised form 17 October 2024; Accepted 18 October 2024
Available online 24 October 2024

guidelines to monitor and regulate CECs, it was only in 2024 that a new Urban Wastewater Treatment Directive (UWWTD) was approved [5]. This directive revises and replaces legislation over 30 years old, introducing new legal requirements for the removal of specific CECs in urban WWTPs. To reduce the release of CECs into surface waters and promote water reuse for agricultural purposes, membrane filtration processes like reverse osmosis (RO) and nanofiltration (NF) are being explored as a viable post-treatment solution for secondary-treated urban wastewater (UWW) [2,6]. However, during the membrane separation process, there is the unavoidable generation of a concentrated stream, also known as retentate, generally characterized by high levels of inorganic salts, refractory organic substances, and trace micropollutants [7,8], that must be treated before discharging to the natural environment.

Advanced oxidation processes (AOPs) have emerged as effective methods to reduce the pollutant load in wastewater matrices and oxidize various CECs [9]. According to Hübner et al. [10], AOPs can be broadly classified into four categories that include ozone-based [11–13], radiation-driven [14–16], catalytic [17,18], and other AOPs [19–21]. In general, AOPs are based on the generation of hydroxyl radicals ($^{\bullet}OH$) as reactive species, recognized as powerful and non-selective oxidants with a remarkable ability to remove a wide range of persistent organic compounds [21]. Nevertheless, in recent years, there has been a growing interest in alternative AOPs that utilize sulfate radicals ($SO_4^{\bullet-}$), collectively termed sulfate radical-based advanced oxidation processes (SR-AOPs) [22]. $SO_4^{\bullet-}$ are equally or even more active than $^{\bullet}OH$ (E^0 ($SO_4^{\bullet-}/SO_4^{2-}$) = 2.5–3.1 V *vs.* NHE; E^0 ($^{\bullet}OH/OH^-$) = 1.8–2.7 V *vs.* NHE) [23], with higher selectivity and longer lifetime (30–40 μs for $SO_4^{\bullet-}$ *vs.* 10^{-3} μs for $^{\bullet}OH$) [24]. $SO_4^{\bullet-}$ can be generated by the activation of persulfates (PS), namely peroxymonosulfate (PMS, HSO_5^-) and peroxydisulfate (PDS, $S_2O_8^{2-}$), through various means, such as radiation (e.g., ultraviolet (UV) light, gamma ray, or ultrasound), transition metals, alkaline or thermal approaches [25–27]. Numerous studies have demonstrated that the combination of PMS and PDS with UV radiation yields highly promising results in the treatment of water and wastewater [28–31]. This approach has shown the capacity to achieve simultaneous removal of various groups of CECs, microorganisms, and organic matter, as well as a superior performance compared to more established AOPs, such as ultraviolet C radiation combined with hydrogen peroxide (UVC/H_2O_2) [32,33]. PS compounds can be readily acquired commercially, e.g., PMS in the form of oxone ($KHSO_5{\cdot}0.5KHSO_4{\cdot}0.5K_2SO_4$) and PDS in the form of sodium peroxydisulfate ($Na_2S_2O_8$), potassium peroxydisulfate ($K_2S_2O_8$) or ammonium peroxydisulfate ($(NH_4)_2S_2O_8$). PDS salts are preferred over PMS salts since they are more stable, environmentally friendly, and cheaper [34]. However, when comparing costs with H_2O_2, the most used oxidant in AOPs for water/wastewater treatment, PDS salts are approximately 10 times more expensive on an equimolar basis [35]. Therefore, *in situ* generation of PS from sulfate (SO_4^{2-}) via electrochemical methods presents a promising alternative, saving costs associated with the separation, purification, transport, and storage of the PS compounds.

Within the framework of the European-funded SERPIC project – Sustainable Electrochemical Reduction of Contaminants of Emerging Concern and Pathogens in WWTP Effluent for Irrigation of Crops – the SERPIC-UCLM® cell was developed. This electrochemical flow cell, designed and built using computational aided design (CAD) and three-dimensional (3D) printing technology, consists of a filter-press configuration equipped with boron-doped diamond (BDD) and stainless-steel (SS) electrodes [36,37]. The SERPIC-UCLM® cell has proven successful application in the electrochemical production of peroxymonosulfuric acid (PMSA, H_2SO_5), also known as Caro's acid, operating in both discontinuous and continuous modes [36,37]. PMSA is generated electrochemically via the anodic oxidation of SO_4^{2-} under strongly acidic conditions, either directly by electron transfer of SO_4^{2-} at the anode surface (Eq. (1)) or indirectly by the interaction of $^{\bullet}OH$ radicals generated at the anode surface with the sulfate species (Eq. (2)) [38]. Potential side reactions, such as i) the electrolysis of water (H_2O), ii) the production of hydrogen (H_2) and H_2O_2 at the cathode surface, and iii) the evolution of oxygen (O_2) and ozone (O_3) at the anode surface, may occur in simultaneous to the production of PMSA, decreasing the efficiency and selectivity of the process [39–43]. Finally, PMSA is a highly reactive peroxyacid that undergoes self-decomposition at neutral pH, primarily existing in the form of PMS [44].

$$H_2SO_4 + H_2O \rightarrow H_2SO_5 + 2H^+ + 2e^- \quad (1)$$

$$SO_4^{\bullet-} + HO^{\cdot} + H^+ \rightarrow H_2SO_5 \quad (2)$$

UV radiation is already applied in many WWTPs as the final treatment stage, so there is potential for its use to activate PS to promote SR-AOPs within these facilities. However, the primary purpose of the UV stage is disinfection, and these systems are not optimized for the effective oxidation of persistent organic pollutants. In this context, the tubular membrane photoreactor (TMPr) developed by Vilar et al. [45] has demonstrated outstanding efficacy in eliminating CECs from secondary-treated UWW at short residence times with the application of several UV-driven AOPs [35,46–48]. This TMPr incorporates four low-pressure UVC lamps distributed externally and equidistant to the photoreactor tube. Additionally, the TMPr design features inlet/outlet pipes tangential to the reactor wall and perpendicular to the liquid flow direction, promoting a helical flow of water around a ceramic tubular membrane located in the center of the reactor. The membrane acts as a longitudinal distributor device by continuously delivering the oxidant through its pores. The fusion of these design elements enables uniform radial and axial delivery of the oxidant along the entire length of the reactor.

This study focuses on integrating the two systems – SERPIC-UCLM® cell and TMPr – in continuous mode operation to promote SR-AOPs for elimination of CECs in highly complex wastewater matrices, specifically RO and NF concentrates (RO_C and NF_C, respectively) obtained from the effluent of a municipal WWTP. First, the SERPIC-UCLM® cell was assessed in terms of mass transport using the limiting current technique with the reversible ferricyanide – ferrocyanide reaction to calculate the volumetric mass transport coefficient (k_mA) and Sherwood number (*Sh*). Subsequently, phototreatments of RO_C/NF_C were carried out in the TMPr using *in situ* electrochemically produced PS from the SERPIC-UCLM® cell and commercially purchased PS salt for comparison. The performance of the phototreatments considered the removal of various CECs, classified as (very-)Persistent/(very-)Mobile/(potentially-)Toxic compounds and selected based on methodologies developed and investigated by Verlicchi et al. [49,50]. The examined CECs included several pharmaceutical compounds – two β-blocking agents: atenolol (ATNL) and bisoprolol (BSPL); carbamazepine (CBZ) and its metabolite carbamazepine 10,11-epoxide (CBZ-EPX); the anti-inflammatory diclofenac (DCF); the X-ray contrast agent iopromide (IOP); three angiotensin II receptor blockers: irbesartan (ISTN), losartan (LSTN), and valsartan (VSTN); the antibiotic sulfamethoxazole (SMX); the antidepressant venlafaxine (VLX); the insect repellent N,N-diethyl-*meta*-toluamide (DEET), the herbicide diuron (DRN), and the flame-retardant melamine (MLN). Of the compounds selected, CBZ, DCF, ISTN, and VLX, are included in the new proposal of UWWTD approved by all EU state members [5]. Furthermore, post-treatment regulatory compliance for discharge into water bodies, particularly regarding pH and chemical oxygen demand (COD), was also under focus.

2. Materials and methods

2.1. Chemicals

In this work, all the reagents were of analytical grade and without further purification. Sulfuric acid (H_2SO_4, VWR Chemicals, 95.0 % purity) was used as the electrolyte in the electrochemical generation of PMSA and as a reagent in the cleaning procedure in determining mass transport parameters. Sodium peroxydisulfate ($Na_2S_2O_8$, Merck, ≥ 99 %

w/w, CAS# 775–27-1) was used as a commercial source for PS. Sodium hydroxide (NaOH, VWR Chemicals, 99.2 % purity) was used for pH adjustment. Potassium iodide (KI, VWR Chemicals, 99.5 % purity) and sodium thiosulfate pentahydrate ($Na_2S_2O_3{\cdot}5H_2O$, Pronalab, purity ≥ 99.5 %) were used as analytical reagents to determine PMSA concentration. Potassium hexacyanoferrate (II) trihydrate ($K_4Fe(CN)_6{\cdot}3H_2O$, VWR Chemicals, purity ≥ 98.5 %), potassium hexacyanoferrate (III) ($K_3Fe(CN)_6$, Alfa Aesar, purity ≥ 98.0 %), and sodium carbonate (Na_2CO_3, Labkem, 99.0 % purity) were used as reagents in the determination of mass transport parameters. Oxalic acid dihydrate ($C_2H_2O_4{\cdot}2H_2O$, Merck, purity ≥ 99.5 %) was used as a reagent in the cleaning procedure in the determination of mass transport parameters. Sodium sulfite (Na_2SO_3, VWR, 98 % purity) was added as quenching agent to stop the oxidation reaction. All solutions were prepared with demineralized water obtained from a reverse osmosis system (Panice®).

2.2. 3D printed electrochemical cell: SERPIC-UCLM® cell

The SERPIC-UCLM® cell was designed and printed using the Fusion 360 Software. This design presented a filter-press configuration that consisted of a 170 mm × 110 mm parallelepiped that beared two 50 mm × 50 mm electrode sockets. These sockets were linked to the fluid inlet and outlet by a conical shape zone (see Fig. 1) for better liquid distribution and evacuation of the generated gas. Additionally, some fins were incorporated at the inlet area to allow a proper liquid distribution throughout the electrode surface. The separation between electrodes was between 5–6 mm, thus ensuring low energy consumption by increasing linear speed with low flow rates. These non-standard features improved traditional reactor configurations, helping to achieve good mass transport and a proper electrode operation, avoiding gas clogging of the surface and gas pockets at the upper parts of the cell. This aspect of the design directly affected mass transport. Although one-compartment configuration was used in this work, the cell can also operate in double-compartment mode with the addition of a membrane. The main features regarding the cell configuration are shown in Table 1. After the design process, the reactor (pieces 1 and 5 in Fig. 1) was made using stereolithography 3D printing technique with a Form 3 machine purchased from Formlabs (PKG-F3-WSVC-BASIC, Germany). The material selected is a translucent acrylic-based resin (Clear Resin V4, Formlabs, Germany) with enough mechanical and chemical resistance to work in the conditions proposed in this work. In the printing process, a thin layer of the resin was squished to a transparent polymer while a focused UV laser photopolymerized the resin layer by layer. As a result, the CAD-designed piece was made with minimal material waste compared with other manufacturing techniques like computer numerical control (CNC) machining. The minimal material waste, together with the low energy consumption of the process, made the reactor fabrication process low-cost and fast. In the current work, BDD and SS plates were used as electrodes. All the details about the BDD electrode were reported by Castro et al. [36]. Afterward, the BDD and SS electrodes were glued to the electrode socket using epoxy resin, and the electric contact was made using cold welding at the back part of the electrode. Finally, the anodic and cathodic reactor parts were merged using a silicone gasket. The stability of the polymerized material was assessed by immersing a small piece in a 1 M H_2SO_4 solution for a duration of 4 weeks. Throughout this period, no noticeable changes in color, mass, and hardness were observed, indicating the resistance of the material to the acidic environment.

Table 1
Main features of the SERPIC-UCLM® cell.

Features	SERPIC-UCLM® cell
Cell height, H_{cell} (mm)	110
Cell length, L_{cell} (mm)	170
Cell area, A_{cell} (cm^2)	18.70
Electrode height, H (mm)	50
Electrode length, L (mm)	50
Inter-electrode gap, S (mm)	5–6
Electrodes active area, A (cm^2)	25
Cross-sectional area, A_c (cm^2)	2.5
Hydraulic diameter, d_H (mm)	9
Active volume, V_a (mL)	12.5
Solution volume, V_S (mL)	500
Electrodes active surface area to solution volume ratio (m^2/m^{-3})	5
Electrodes active surface area to active volume ratio (m^2/m^{-3})	200
Anode material	BDD[a]
Cathode material	SS[b]

[a] The BDD electrode was used as anode for the electrochemical generation of PMSA, and it was used as cathode for the mass transport assessment essays.
[b] The SS electrode was used as cathode for the electrochemical generation of PMSA, and it was used as anode for the mass transport assessment essays.

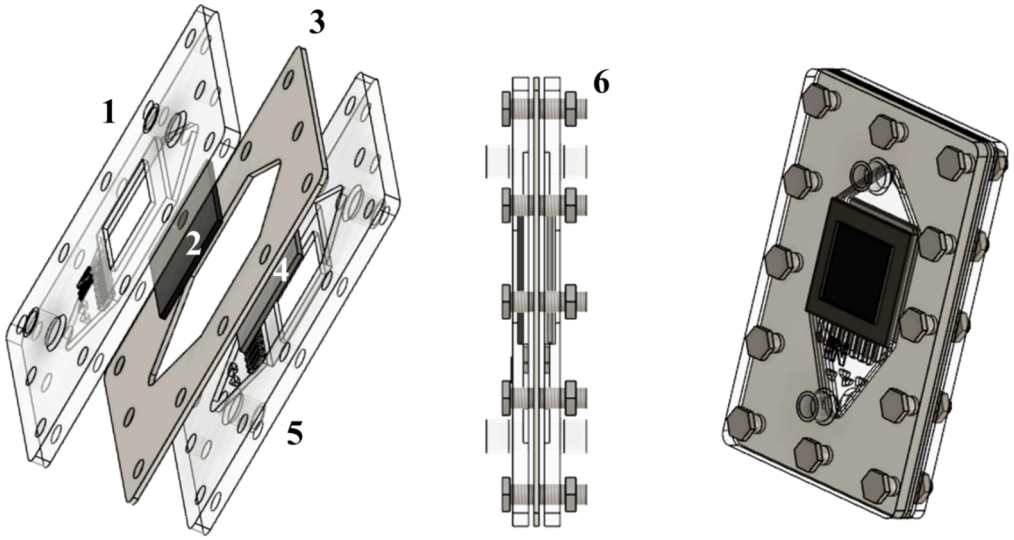

Fig. 1. SERPIC-UCLM® cell designed in an exploded, lateral, and orthogonal view. Numbers correspond to the different parts. 1) Inlet and anodic socket, 2) BDD electrode, 3) Silicone gasket, 4) SS cathode, 5) Outlet and cathodic socket, 6) Perimetral screws.

2.3. Mass transport assessment: SERPIC UCLM® cell

2.3.1. Electrochemical setup

The electrochemical setup for the mass transport assessment mainly consisted of (i) 1 L capacity glass vessel thermostatically controlled (TCH5 Surcis), (ii) SERPIC-UCLM® cell equipped with BDD and SS electrodes as cathode and anode, respectively, (iii) gear pump (Watson-Marlow 502S), and (iv) power supply (Velleman®, model LABPS3005DN, 0 – 5 A, 0 – 30 V). All the electrochemical system was connected by polytetrafluoroethylene (PTFE) tubing.

2.3.2. Experimental procedure

Mass transport characterization of the SERPIC-UCLM® cell was determined by the limiting-current technique for the ferrocyanide $\left(Fe(CN)_6^{4-}\right)$ – ferricyanide $\left(Fe(CN)_6^{3-}\right)$ reversible reaction (Eq. (3)) [51]. This reaction was taken to the maximum achievable rate, at which point mass transfer became the rate-limiting step.

$$Fe(CN)_6^{3-} + e^- \leftrightarrow Fe(CN)_6^{4-} \qquad E^0 = 0.358 Vvs.SHE \tag{3}$$

The experimental methodology was based on Selman and Tobias [52]. A solution was prepared by spiking demineralized water with 10 mM $K_3Fe(CN)_6$, 100 mM $K_4Fe(CN)_6$ (reactant in excess to guarantee the occurrence of the limiting reaction in the cathode), and 0.5 M Na_2CO_3 (supporting electrolyte). A solution volume of 1 L was put into the recirculation vessel protected from light with aluminum foil. Then, the solution was recirculated between the vessel and the reactor (operation semi-batch mode) until reaching a temperature of 25 ± 1 °C. Flow rates of 10 – 70 L h^{-1} were applied. Current intensity *vs*. potential curves were recorded by applying a potential scanning with small increments of 0.05 V or 0.1 V. Curves exhibited three regions: (i) a region with increasing current intensities for increasing potentials, in which the $Fe(CN)_6^{3-}$ – $Fe(CN)_6^{4-}$ reaction rate was controlled by mass and charge transfer, (ii) a region with a constant current intensity for rising potentials – the limiting current intensity (I_L), in which the $Fe(CN)_6^{3-}$ – $Fe(CN)_6^{4-}$ reaction was under mass transfer control, and (iii) a region with a dramatic increase in the current intensity for increasing potentials as a result of the occurrence of secondary reactions. The potential scanning was carried out until the resulting current intensity increased sharply. The cathode was cleaned and activated before each experiment by applying a current density of 10 mA cm^{-2} for 15 min to 0.5 M Na_2CO_3 solution under recirculation in the system. Furthermore, the system was additionally cleaned at every two experiments by recirculating 20 mM oxalic acid dihydrate ($C_2H_2O_4{\cdot}2H_2O$) for 15 min, 1 M of H_2SO_4 for 15 min, and demineralized water for 15 min.

2.3.3. Calculations

The I_L (A) was used to determine the volumetric mass transport coefficient k_mA (s^{-1}) via Eq. (4)) [53 54], where n is the stoichiometric number of electrons consumed in the electrode reaction (one exchanged electron for the $Fe(CN)_6^{3-}$ – $Fe(CN)_6^{4-}$ reaction), F is the Faraday constant (96,485 C mol^{-1}), C_{BS} is the concentration of $Fe(CN)_6^{3-}$ in the solution (mol m^{-3}), A is the interfacial area per unit of volume and represents the ratio between the active electrode surface (A_a, m^2) and the active volume (V_a, m^3). This equation considers that the rate of mass transport equals that of electricity exchange according to Faraday.

$$k_mA = \frac{I_L}{nFV_aC_{BS}} \tag{4}$$

Moreover, k_mA was determined by employing an empirical correlation presented in Eq. (5) [53],

$$k_mA = qv_{avg}^b \tag{5}$$

where q and b are empirical constants, which depend on the reactor geometry and hydrodynamics regime within the reactor, respectively [55]. The mean linear velocity, v_{avg} (m s^{-1}), is obtained by relating the electrolyte flow rate Q (m^3 s^{-1}) with the cross-sectional area A_c (m^2) as expressed in Eq. (6).

$$v_{avg} = \frac{Q}{A_c} \tag{6}$$

The dimensionless Sherwood number (*Sh*) was calculated via Eq. (7) [56], where d_h is the hydraulic diameter (m) calculated via Eq. (8), D is the molecular diffusion coefficient of $Fe(CN)_6^{3-}$ (6.4×10^{-10} m^2 s^{-1} [57]), and P is the perimeter (m).

$$Sh = \frac{k_m d_h}{D} \tag{7}$$

$$d_h = \frac{4A_c}{P} \tag{8}$$

Moreover, *Sh* was determined by the dimensional analysis presented in Eq. (9). For electrochemical reactors, the coefficient c is associated with the value of 1/3, obtaining the following expression [57]:

$$Sh = aRe^bSc^c = aRe^bSc^{1/3} \tag{9}$$

The parameters a and b can be determined by non-linear fitting of the empirical results. The coefficient a is related to the reactor geometry, size, and inter-electrode gap. The coefficient b is related to the hydrodynamics fluid behavior. Note that the coefficient b is the same for both k_mA and *Sh* correlations.

The *Sh* was calculated as a function of the Reynolds number (*Re*), which was determined via Eq. (10) [58], where Q is the solution flow rate (m^3 s^{-1}), ν is the solution kinematic viscosity (m^2 s^{-1}), and A_c cross-sectional area of the reactor channel (m^2).

$$Re = \frac{Qd_h}{\nu A_c} \tag{10}$$

2.4. Electrochemical generation of PMSA

The electrochemical generation of PMSA was performed using the SERPIC-UCLM® cell equipped with a BDD electrode as anode and a SS electrode as cathode. The electrochemical process consisted of the oxidation of 1 M of H_2SO_4 (1 L), used as substrate and supporting electrolyte. The process was carried out in continuous operational mode. An electrolyte flow rate of 50 L h^{-1} was recirculated between a 1 L cylindrical glass vessel to the electrochemical cell and a heat exchanger using a peristaltic pump (Watson-Marlow 502S). Simultaneously, a peristaltic pump (Watson-Marlow 120S) with a flow rate of 33 mL h^{-1} was used to feed the cylindrical glass vessel with fresh electrolyte and remove the generated PMSA from the system. The temperature was kept at 20 ± 1°C using a thermostat bath (TCH5 Surcis). Both electrodes were connected to a power supply (Velleman®, model PS3020, 0 – 20 A, 0 – 30 V), providing a current density (j) of 300 mA cm^{-2}. The initial electrolyte pH was adjusted with NaOH. At intervals of 15 min, 5 mL of the sample was taken out of the glass vessel to determine the PMSA concentration by an iodometric titration method according to Castro et al. [36]. The experimental setup for the electrochemical generation of PMSA is shown in Fig. 2a.

2.5. Production and characterization of the RO_C and NF_C

The production of the RO_C and NF_C was carried out in a pilot membrane filtration unit (RO-250 Model, Aquaquímica, Lda, Portugal) implemented in a municipal WWTP, located in the North of Portugal. The unit consists of an EFAFLU pump (model BMV 2–18, 2.2 kW, 320 V) operating with pressures between 7 and 15 bar and a maximum permeate flow rate of 250 L h^{-1}. RO or NF membranes (RE 4040-BE or NE 4040–70, CSM) were used to produce the concentrates. A 20 μm cartridge filter was installed to pre-filter the UWW entering the

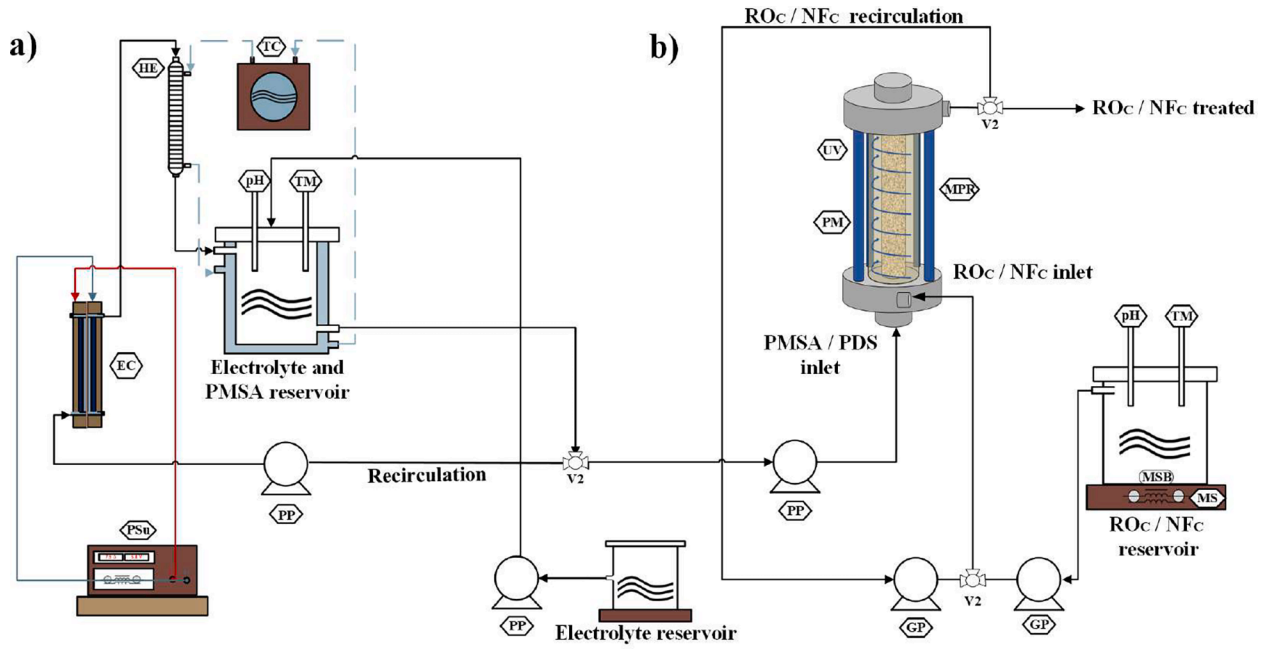

Fig. 2. Sketch of the setup integrating the SERPIC-UCLM® cell with the tubular membrane photoreactor (TMPr), applied in continuous mode operation for the phototreatment of RO_C and NF_C. Legend: EC: electrochemical cell, GP: gear pump, HE: heat exchanger, MS: magnetic stirrer, MSB: magnetic stirrer bar, MPR: membrane photoreactor, pH: pH-meter, PM: permeation membrane, PP: peristaltic pump, PSu: power supply, TC: temperature controller, TM: temperature meter, UV: UVC lamps, and V2: two-way valve.

membrane unit as well as two sand containers (9 3/4'' each, APAH6 (3 – 8 mm) followed by APAH4 (2 – 4 mm), Aquaquimica, Portugal) for post-filtration of the produced concentrate, to reduce the content of particulate matter. The UWW was collected downstream of the second clarifier, stored in a 1 m^3 capacity feed tank and pumped (MEW pump QB-70, 230 V, 550 W, maximum flow rate of 40 L min^{-1}) to the RO/NF unit. The concentrate was reintroduced into the feed tank until reaching a final volume of 375 L (concentration factor ≈ 2.7). From then onward the concentrate was collected in a storage tank (≈ 100 L). The characterization of the RO_C and NF_C samples used in the photo-oxidation tests, as well as the respective analytical equipment/methods, are detailed in Table 2.

2.6. Photodegradation tests

2.6.1. Photoreactor setup

All photo-oxidation tests were carried out in a lab-scale TMPr. A sketch of the phototreatment setup is shown in Fig. 2b. Briefly, the TMPr comprises an inner ceramic ultrafiltration membrane (γ-Al_2O_3 membrane from Inopor® GmbH, Germany; cut-off = 20 kDa; pore size = 10 nm; porosity = 30–55 %; $Ø_{external}$ = 20 mm; $Ø_{internal}$ = 16 mm; total length = 200 mm; illuminated length = 174 mm) and an outer quartz tube (from E.VILA Projects & Supplies SL, Spain; $Ø_{external}$ = 42 mm; $Ø_{internal}$ = 38 mm; total length = 200 mm; illuminated length = 174 mm). The effluent to be treated was continuously pumped through a gear pump (Ismatec BVP-Z) from a cylindrical glass vessel to the reactor and is partially recirculated back to the TMPr using another gear pump (Ismatec BVP-Z). A peristaltic pump (Shenchen LabK1) was used to dosage the oxidant stock solution to the photoreactor's annular reaction zone (ARZ). Four UVC lamps (Puritec HNS 11 W G5 from Osram) were inserted equidistantly outside the quartz tube (photon flow of 2.3 ± 0.2 W, according to ferrioxalate actinometry), and a square capsule covered with aluminum foil enclosed the experimental installation, promoting light reflection and preventing eye contact with the light source.

2.6.2. Phototreatment procedure

Photo-oxidation tests were performed with RO_C or NF_C under natural pH and without CECs fortification, applying a feed flow (Q_F) of 2.5 L h^{-1} and recirculation flow (Q_R) of 27.5 L h^{-1} (equivalent to a residence time (RT) of 3.4 min and a flow in the annular reaction zone (Q_{ARZ}) of 30 L h^{-1}) under UVC radiation (3.3 kJ L^{-1}). The oxidant stock solution was electrochemically generated by the SERPIC-UCLM® cell or prepared from commercial $Na_2S_2O_8$, which among the PDS salts is considered the most suitable for water and wastewater treatment [34]. Table 3 summarizes the experimental conditions applied in the photo-oxidation tests.

In a regular operation, the TMPr was initially filled with the oxidant stock solution, which, during the phototreatment and at a pre-defined rate, was forced to permeate through the membrane pores (radial permeation) to be delivered to the ARZ where the RO_C/NF_C flows. The photo-oxidation tests started with the simultaneous activation of the pumps for feeding and recirculating the RO_C/NF_C to the reactor, the UVC lamps, and the peristaltic pump that doses the oxidant. Under steady-state conditions, at least three samples from TMPr outlet were collected for analysis and characterization. To avoid oxidation after sampling, a solution of Na_2SO_3 was immediately added to the samples in a 5:1 M ratio considering the oxidant dose.

2.7. Statistics analysis

Statistical analyses were conducted using R Studio. Initially, data was screened for outliers using Grubb's test (at a 5 % significance level). Differences between 1.2 mM PMSA and 1.2 mM PDS in the RO_C were evaluated using a *t*-test, while differences between 1.2 mM PMSA–1.2 mM PDS and 1.2 mM PMSA–2.4 mM PMSA in the NF_C were assessed with a one-way ANOVA followed by Tukey's post-hoc test. Normality (Kolmogorov–Smirnov test) and homogeneity of variances (Levene's test) were checked, and data transformation was applied as needed to meet analysis assumptions. When normality and/or homogeneity were violated, a non-parametric test was used, followed by Dunn's post-hoc comparison. Significance levels were indicated as follows: −*for *p*-value ≤ 0.05, ** for *p*-value ≤ 0.01, *** for *p*-value ≤ 0.001.

Table 2
Characterization of the RO_C and NF_C produced by membrane filtration of UWW after secondary treatment.

Analytical equipment/ method	Parameter	Units	RO_C	NF_C
Hanna Instruments HI8424	pH	–	7.6	7.9
Hanna Instruments Edge HI2003-02	Conductivity	μS cm^{-1}	5700	2315
Dichromate closed reflux method according to the 5220 D test [83]	Chemical Oxygen Demand (COD)	mg L^{-1}	195	206
Non-dispersive infrared (NDIR) spectrometry in a TOC-V_{CSN} analyzer from Shimadzu	Dissolved Organic Carbon (DOC)	mg L^{-1}	48	51
	Dissolved Inorganic Carbon (DIC)	mg L^{-1}	178	65
According to the 2540 D and 2540C test [83]	Total Suspended Solids (TSS)	mg L^{-1}	52	12
	Total Dissolved Solids (TDS)	mg L^{-1}	1883	1092
Ion chromatography using a Dionex ICS-2100 LC equipped with an IonPac® AS11-HC 250 mm x 4 mm column and an anion self-regenerating suppressor ASRS® 300, 4 mm; and Dionex DX-120 LC equipped with an IonPac® CS12A 250 mm x 4 mm column at ambient temperature and a cation self-regenerating CSRS® Ultra II, 4 mm.	Chloride (Cl^-)	mg L^{-1}	689	232
	Nitrate (NO_3^-)	mg L^{-1}	9.9	19.1
	Nitrite (NO_2^-)	mg L^{-1}	25.2	18.8
	Sulfate (SO_4^{2-})	mg L^{-1}	315	298
	Phosphate (PO_4^{3-})	mg L^{-1}	44.2	43.1
	Ammonium (NH_4^+)	mg L^{-1}	223	53.8
	Potassium (K^+)	mg L^{-1}	196	84.3
	Sodium (Na^+)	mg L^{-1}	855	422
	Calcium (Ca^{2+})	mg L^{-1}	128	112
	Magnesium (Mg^{2+})	mg L^{-1}	36.0	99.0
Acquity UPLC® liquid chromatograph interfaced to a XEVO TQD® triple quadrupole mass spectrometer equipped with an electrospray interface (ESI) from Waters (Milford, MA, USA) [52]	Atenolol (ATNL)	μg L^{-1}	0.2	<0.18
	Bisoprolol (BSPL)	μg L^{-1}	1.3	1.7
	Carbamazepine (CBZ)	μg L^{-1}	2.4	3.4
	CBZ 10,11-epoxide (CBZ-EPX)	μg L^{-1}	0.5	0.9
	DEET (DEET)	μg L^{-1}	2.2	<0.05
	Diclofenac (DCF)	μg L^{-1}	6.5	8.5
	Diuron (DRN)	μg L^{-1}	0.2	0.3
	Iopromide (IOP)	μg L^{-1}	18.6	16.0
	Irbesartan (ISTN)	μg L^{-1}	4.2	8.6
	Losartan (LSTN)	μg L^{-1}	3.6	2.8
	Melamine (MLN)	μg L^{-1}	20.5	10.5
	Sulfamethoxazole (SMX)	μg L^{-1}	0.8	1.3
	Valsartan (VSTN)	μg L^{-1}	5.5	<0.17
	Venlafaxine (VLX)	μg L^{-1}	2.4	2.3

3. Results and discussions

3.1. Mass transport in SERPIC-UCLM® cell

This section provides a rigorous and exhaustive study of the mass transport features (k_mA and *Sh* values) of the SERPIC-UCLM® cell, including all pertinent information not previously addressed by Castro et al. [37]. This novel customized cell achieved k_mA values rising from $(4.8 \pm 0.1) \times 10^{-3}$ s^{-1} to $(11.76 \pm 0.02) \times 10^{-3}$ s^{-1}, and *Sh* values rising from 343 ± 8 to 835 ± 2, for *Re* values ranging from 110 to 790 (1.1×10^{-2} m $s^{-1} < v_{avg} < 7.8 \times 10^{-2}$ m s^{-1}, and 10 L $h^{-1} < Q < 70$ L h^{-1}) (Fig. 3**a**). The mass transport enhancement for increasing *Re* from 110 to 790 was about 2.4-fold in k_mA and *Sh* values. This behavior can be mainly attributed to the decrease in the diffusion boundary layer, shortening the diffusion distance and improving mass transport by diffusion forces from the bulk solution to the electrode surface [53].

Fig. 3**b** exhibits the empirical data of k_mA as a function of the v_{avg} from Eq. (5). This correlation depends on multiple factors, including the electrode geometry and thickness, the electrolyte transport properties, and process conditions [59]. The empirical coefficients *q* and *b* provide valuable insights regarding the cell mass transport features. For instance, coefficient *q* is related to the electrode properties [59]. A higher value of *q* likely indicates higher mass transport features. The coefficient *b* is related to the hydrodynamics behavior of the fluid within the cell. In this work, the value of *b* may be affected by the cone-shaped inlet finished with rectangular distribution fins. This design promotes turbulence in the fluid stream by creating zones of microturbulence close to the electrode surface, thus increasing the mass transport.

Fig. 3**c** displays the dimensional *Sh* correlation (Eq. (9) as a function of hydrodynamics (*Re*) and the electrolyte transport properties (*Sc*). The empirical coefficient *a* is primarily related to the reactor geometry and size [60]. The proposed cell design achieved a relatively large value of *a* (equal to 2.59 ± 0.06), indicating a clear superiority in mass transport. This outcome can be attributed to several factors: i) the filter-press cell design incorporating a conical-shaped inlet for an optimal flow distribution and efficient gas evacuation to prevent gas bags within the cell (see *section 2.2*), ii) the narrow inter-electrode gap (5–6 mm) leading to shorter pathways between the bulk solution and the electrode surface, and finally iii) the low cell volume facilitating high linear velocity in the fluid with minimal power pumping. Note that the constant *b* is equal for both *Sh* and k_mA correlations.

3.1.1. SERPIC-UCLM® cell versus literature

The mass transport features (k_mA and *Sh*) of the SERPIC-UCLM® cell were compared to those of various electrochemical reactor configurations and electrode materials reported in the literature (Fig. 4 and Fig. 5). The pertinent information utilized in this section can be found in Table SM-1 and Table SM-2. Fig. 4 depicts a log–log plot of k_mA *vs.* v_{avg} between the SERPIC-UCLM® cell and the electrochemical systems reported in the literature. Results from this study showed satisfactory mass transport rates. These k_mA values were superior to those obtained by Arenas et al. [61] using plate and mesh electrodes, but not as high as those obtained by Langlois et al. [62] for foam electrodes and by Abahussain et al. [63] for a felt electrode. Despite the better performance of foam and felt electrodes, a fundamental limitation of these materials is the difficulty of achieving a uniform current density distribution, which can lead to decreased process efficiency and selectivity Abahussain et al. [63]. In the study by Abahussain et al. [63], replacing felt and fine mesh electrodes with a flat plate electrode led to much lower k_mA values, which were lower than those observed in the SERPIC-UCLM® cell. While Abahussain et al. [63] applied a flat plate reactor with a simple conical-shaped inlet/outlet, the SERPIC-UCLM® cell incorporates some fins in the conical-shaped inlet, which are responsible for a better liquid distribution across the electrode surface. In addition, the k_mA values

Table 3
Experimental conditions applied in the photo-oxidation tests and physicochemical characterization of the RO_C and NF_C at the end of the phototreatments.

Test (#)	Concentrate	PS production	$[PS]_{stock}$ (mM)	$[PS]_{ARZ}$ (mM)	pH	COD (mg L^{-1})	DOC (mg L^{-1})	TSS (mg L^{-1})
1	RO_C	Electrochemical	267.5	1.2	7.4	195	46	45
2		Commercial		1.2	8.1	174	46	35
3	NF_C	Electrochemical	241.3	1.2	7.5	181	55	19
4		Commercial		1.2	7.6	143	54	20
5		Electrochemical		2.4	6.8	116	51	11

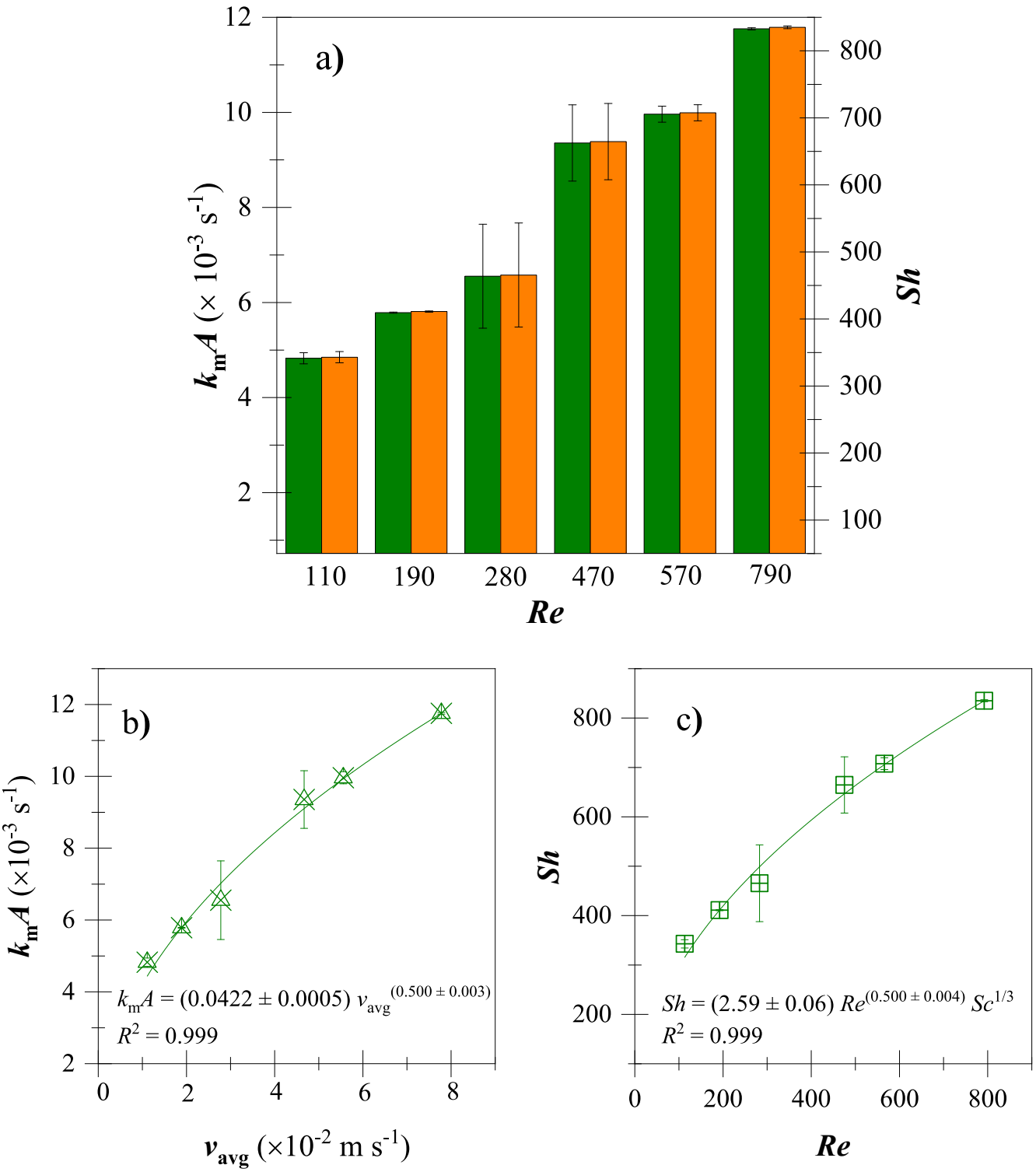

Fig. 3. Mass transport assessment in the SERPIC-UCLM® cell: a) k_mA ( ) and *Sh vs. Re* ( ), b) k_mA *vs.* v_{avg} ($k_mA = q\ v_{avg}{}^b$), and c) *Sh vs. Re* ($Sh = a\ Re^b\ Sc^{1/3}$). Working conditions: 110 < *Re* < 790 (10 L h^{-1} < *Q* < 70 L h^{-1}, and 1.1 × 10^{-2} m/s < v_{avg} < 7.8 × 10^{-2} m/s), *Sc* = 1494, [$K_3Fe(CN)_6$] = 10 mM, [$K_4Fe(CN)_6$] = 100 mM, [Na_2CO_3] = 0.5 M, and *T* = 25 ± 1 °C.

obtained by the SERPIC-UCLM® cell were surpassed by the electrochemical flow reactor equipped with the NETmix static mixer on the electrode surface, as reported by Morais et al. [64]. Incorporating the NETmix static mixer can significantly enhance mass transport rates by increasing the convective mixing effects alongside the static mixer structure [64]. However, the intricate design of these static mixers can be a remarkable limitation when it comes to cost-effective production employing conventional manufacturing.

Fig. 5 depicts the log–log plot of $Sh\ Sc^{-1/3}$ *vs. Re* between the SERPIC-UCLM® cell and several electrochemical systems reported in the literature. The $Sh\ Sc^{-1/3}$ values are preferred over the *Sh* values to discard the effect of the *Sc* when comparing the *Sh* correlations. The SERPIC-UCLM® cell performed similarly to most electrochemical systems reported in the literature, outperforming the well-known DiaCell® reactor

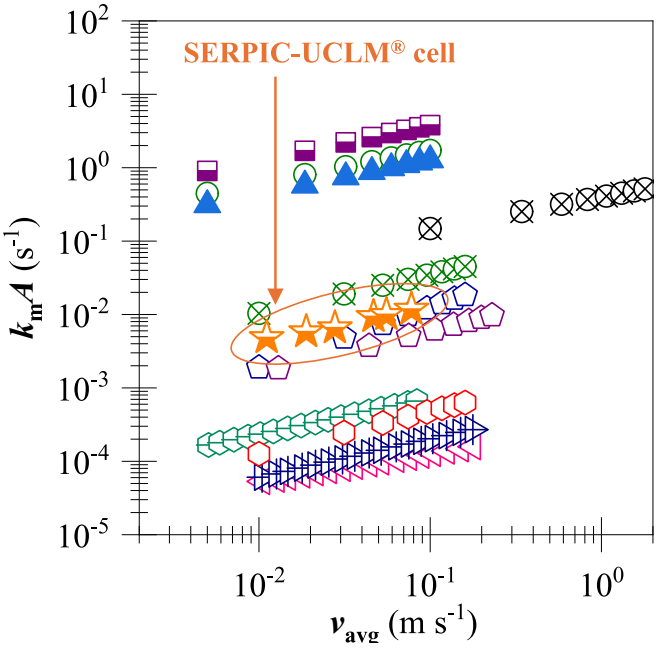

Fig. 4. Volumetric mass transport coefficients (k_mA) of empirical data (SERPIC-UCLM® cell) and literature data from distinct electrochemical systems as a function of mean linear velocity (v_{avg}). Legend: SERPIC-UCLM® cell (, this work); Customized cells ([61] with Pt/Ti plate 2D, [61] with Pt/Ti plate + 1 TP, [61] Pt/Ti mesh, [63] with Pt-Ir/Ti plate, [63] with Ti fine mesh, [63] with Pt-Ir/ Ti felt, [62] with Ni foam G45, [62] with Ni foam G60, [62] with Ni foam G100); commercial MicroFlowCell ([64]); e$^-$ NETmix ([64]).

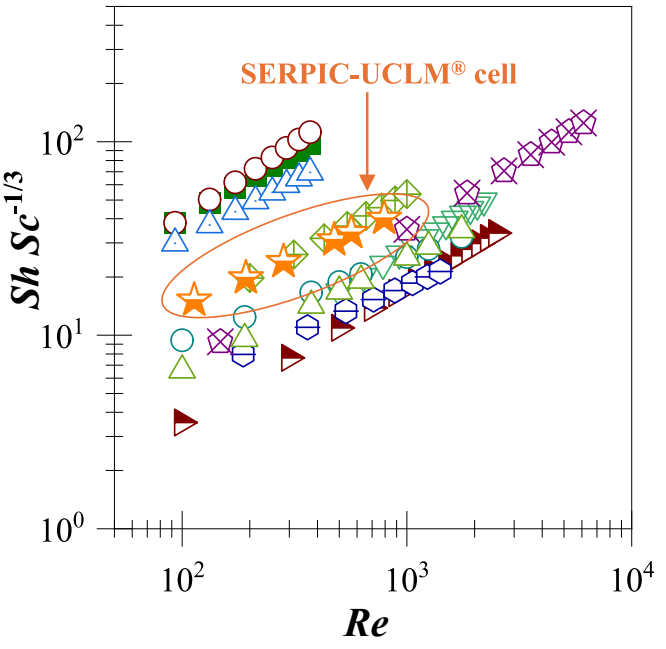

Fig. 5. Sherwood number (Sh) and Schmidt number (Sc) correlation (Sh Sc$^{-1/3}$) of empirical data (SERPIC-UCLM® cell) and literature data from distinct electrochemical systems as function of Reynolds number (Re). Legend: SERPIC-UCLM® cell (this work); DiaCell® ([65]); FM01-LC reactor ([66], [57], [81] with Ni electrodes and without TP); parallel plate reactor ([82]); 3D-printed electrochemical reactor with Ni electrodes ([67] with diamond-shaped 3D-printed TP, [67] with square-shaped 3D-printed TP, [67] with Ni foam 3D electrode); commercial MicroFlowCell ([64]); e$^-$ NETmix ([64]).

[65] and the FM01-LC filter-press electrolyzer [57,66]. This outcome highlights the enhanced design features of the SERPIC-UCLM® cell. Nevertheless, the 3D-printed filter-press reactor with distinct configurations reported by Márquez-Montes [67] surpassed the performance of SERPIC-UCLM® cell. This can be attributed to the electrode geometries and nature (porous electrodes) and the straightforward TP designs (diamond-shaped and square-shaped 3D-printed TPs). The improved performance of the porous electrodes in terms of mass transport has already been proven, being unquestionably evident. Finally, Table SM-2 exhibits an extended range of *a* values, indicating the variety of the reactor designs, including the geometry, size, and inter-electrode gap between the electrochemical systems. For instance, the SERPIC-UCLM® cell achieved a *a* value 18.4-fold higher than the coefficient value obtained by Santos et al. [65] employing the commercially available reactor DiaCell®. In contrast, the coefficient *b* obtained in this work aligns closely with the values reported for other reactor configurations, suggesting a similar dependency on mass transport in the hydrodynamics behavior.

3.2. Integration of SERPIC-UCLM® cell with TMPr

3.2.1. Characteristics of RO_C and NF_C

The composition of raw water, operational parameters, and overall system elements collectively influence the quality and quantity of concentrate produced in membrane processes. Although specific conditions may vary, certain typical trends can be expected. For instance, higher conductivity values are typically observed in RO_C compared to NF_C since RO membranes reject both mono- and multivalent ions, while NF membranes mainly prevent the passage of multivalent ions. This can be easily inferred from the characterization of the concentrates used in this work, as outlined in Table 2, where monovalent ions like chloride (Cl^-) and ammonium (NH_4^+) are 3 and 4 times more concentrated in the RO_C than in NF_C, whereas sulfate (SO_4^{2-}), phosphate (PO_4^{3-}), and calcium (Ca^{2+}) present similar concentrations in both matrices.

Concerning CECs content, all 14 compounds evaluated in this work were detected and quantified in the RO_C ($\sum_{14CECs}$ = 68.9 μg L^{-1}), whereas in the NF_C, 11 CECs were found ($\sum_{11CECs}$ = 56.3 μg L^{-1}), with ATNL, DEET, and VSTN concentrations below the limit of quantification (LQ, Table 2 and Table SM-3). The primary physicochemical characteristics and native concentrations of target CECs of the secondary UWW that generated the RO_C and NF_C are detailed in Table SM-4. Regarding the CECs content, it was observed that the concentrations in the RO_C and NF_C are approximately 6 and 4 times higher compared to the initial concentrations in the influents, respectively. In both concentrates, the non-ionic X-ray contrast agent IOP and the flame-retardant MLN displayed the highest concentrations, while the herbicide DRN and the metabolite CBZ-EPX showed the lowest values (Table 2). It is important to note that both matrices have COD values exceeding the limit stipulated for discharge into receiving water bodies, as established in Directive 91/271/EEC (COD < 125 mg O_2 L^{-1}) [68]. The

noncompliance with this parameter further underscores the necessity to treat these matrices effectively before discharge.

3.2.2. Operational adjustments

Initial phototreatment tests were conducted in the TMPr using RO_C with a continuous dosage of 1.2 mM PMSA electrogenerated by the SERPIC-UCLM cell®, employing the 1 M H_2SO_4 solution without adjustment of the initial pH (pH ~ 0). At the end of the phototreatment, the effluent pH was <6.0, not complying with the limits for discharge into aquatic systems stipulated in Directive 91/271/EEC [34] (6 < pH < 9). The applied acidic PMSA solution could surpass the inherent buffering capacity of the RO_C matrix, conferred by the inorganic carbonaceous matter content, leading to a sudden decline in the final pH. It is imperative to adjust the pH of the PMSA solution not only to ensure an environmentally acceptable pH range in the treated effluent, but also to safeguard the structural integrity and functionality of the ceramic membrane of the TMPr, which acts as a radial distributor of the oxidant. Considering these issues, the initial pH of the electrolyte used to produce PMSA electrochemically was optimized (Fig. 6).

Fig. 6 illustrates the electrochemical production of PMSA at different initial pH values (0.5, 1.0, and 1.5), including a control test without any pH adjustment of the 1 M H_2SO_4 solution (pH of ~ 0) (Fig. 6a) and the pH evolution over the reaction time (Fig. 6b). In the experiment using the electrolyte with an initial pH of 1.5, a gradual increase in pH was observed, followed by a drastic shift from acidic to alkaline conditions, reaching a pH of 12.6 at 180 min. This sharp pH change may be associated with the higher rate of H^+ consumed at the cathode compared to the rate of H^+ produced at the anode, increasing the pH of the solution [69]. In tests using the electrolyte with an initial pH of ~ 0, 0.5, and 1.0, the pH variations were slight, consistent with those achieved in Castro et al. [37], reaching final pH values of the PMSA solution of 0.2, 1.0, and 1.5, respectively. The concentration of PMSA electrogenerated was in the same range among the tests for all initial pH values (~0, 0.5, 1.0, and 1.5) (238 ± 18 mM, Fig. 6a). This observation suggests that altering the initial pH of the electrolyte does not affect significantly the efficiency of PMSA production (Dunn's Test; p-value > 0.05). An initial electrolyte pH of 1.0 was chosen for the electrochemical production of PMSA, intended for subsequent phototreatment tests. This pH value was selected as it resulted in a PMSA solution with a maximum concentration and a final pH that may ensure that the effluent's pH remains within acceptable legal limits after phototreatment, while also enhancing membrane durability.

It should be noted that the generation of PMSA using the SERPIC-UCLM® cell was assessed in terms of the initial concentration of H_2SO_4 in Castro et al. [36,37]. The efficiency in the production of the PMSA proved to be directly related to the concentration of H_2SO_4 in the raw matter. An increment in the initial H_2SO_4 concentration increased the production efficiency of the PMSA since a higher quantity of $SO_4^{2-\bullet}$ was available to produce PMSA. However, very high H_2SO_4 contents led to a decrease in the quality of the final product formed due to the large remaining concentration of electrolyte (H_2SO_4, and its ionic species HSO_4^- or SO_4^{2-}). Therefore, a concentration of 1 M of H_2SO_4 was selected as optimal to produce PMSA and connect the electrochemical system with the phototreatment of CECs.

3.2.3. Activation mechanisms of PMSA/PMS and PDS and their interaction with CECs

According to Ball and Edwards [44], the decomposition of PMSA in aqueous solution can occur spontaneously or by reacting with trace metal catalysts. The first path depends on the pH of the aqueous medium. When pH ranging from 6 to 8, PMSA primarily exists in the form of HSO_5^- and, at more alkaline pH levels (10.5 < pH < 11.7), H_2SO_5 predominantly exists in the form of conjugated base of PMS (SO_5^{2-}) [44]. Given that the pH of RO_C and NF_C is approximately neutral (7.6 and 7.9, respectively), it is assumed that PMSA undergoes self-decomposition, giving rise to PMS. This species becomes predominant in the

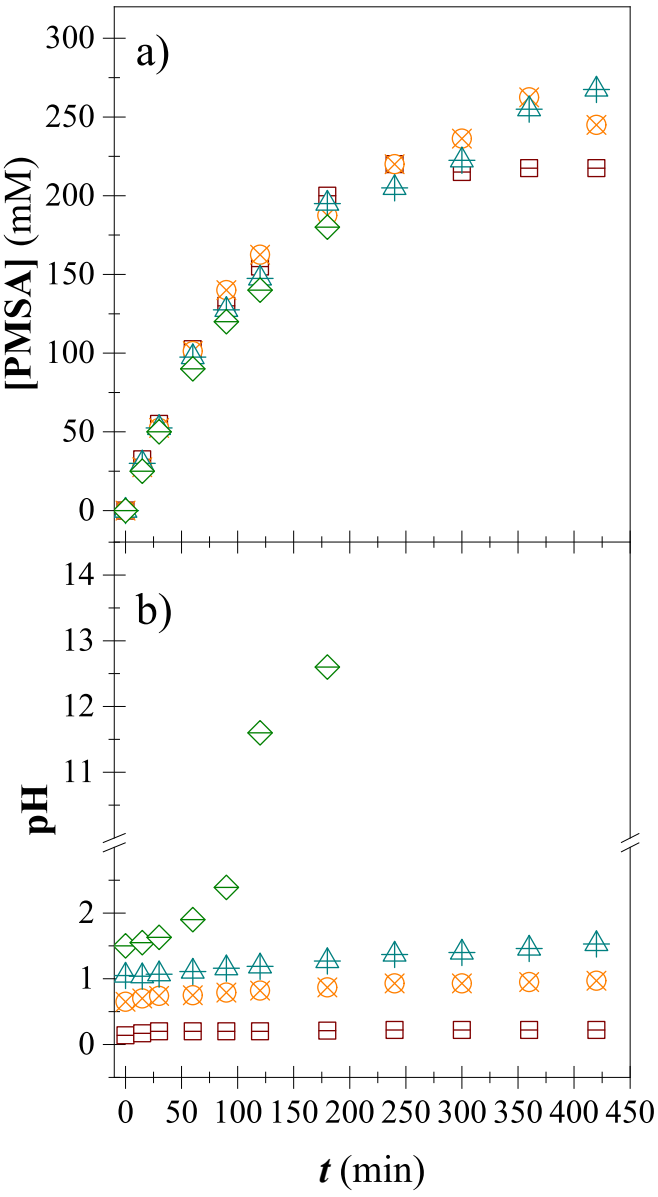

Fig. 6. Effect of the initial pH on the electrochemical generation of PMSA. Legend: initial pH without any adjustment (▭) pH 0.5 (⊠), pH 1.0 (△), and pH 1.5 (◇). Working conditions: $[H_2SO_4]$ = 1 M, j = 300 mA cm $^{-2}$, T = 20 ± 1 °C.

phototreatment of RO_C and NF_C and can be effectively activated by UVC radiation following Eq. (11). Consequently, both $SO_4^{\bullet-}$ and $^\bullet$OH radicals are expected to be generated, whereas the photolysis of PDS only gives rise to $SO_4^{\bullet-}$ radical (Eq. (12).

$$HSO_5^- + h\nu \rightarrow SO_4^{\bullet-} + HO^\bullet \quad (11)$$

$$S_2O_8^{2-} + h\nu \rightarrow 2SO_4^{\bullet-} \quad (12)$$

$^\bullet$OH and $SO_4^{\bullet-}$ radicals can react with organic contaminants through three main mechanisms, including i) electrophilic addition to π bonds, targeting unsaturated or aromatic organic compounds [70], ii) hydrogen abstraction in aliphatic molecules, especially near electronegative groups, leading to oxidative chain reactions [71], and iii) electron transfer, oxidizing organic compounds into charged intermediates, particularly in halogenated hydrocarbons or compounds with significant stereochemical hindrance [70]. $SO_4^{\bullet-}$ radicals mainly react through electron transfer, forming cationic organic radicals. Although hydrogen

abstraction and addition to double bonds also occur with $SO_4^{\bullet-}$ radicals, these pathways contribute less to their overall reactivity compared to $^{\bullet}OH$ radicals, demonstrating the more selective nature of $SO_4^{\bullet-}$ radicals in advanced oxidation processes [72–75].

3.2.4. Phototreatments with electrogenerated vs. commercial PS

After establishing the initial pH of the electrolyte, photo-oxidation tests were conducted on the RO_C. A continuous dosage of 1.2 mM PS was applied, derived from both *in situ* production by the SERPIC-UCLM® cell (PMSA, test #1) and commercially acquired (PDS, test #2). Overall, both tests obtained similar degradation patterns (Fig. 7a), with an average concentration decrease for the 14 CECs present in the RO_C of 37 % (test #1) and 47 % (test #2). The anti-inflammatory DCF presented high oxidation levels, with concentrations falling below the LQ in both tests, resulting in removals $\geq$ 92 %, followed by IOP with degradations ~80 %. The contaminants ATNL, CBZ-EPX, DRN, LSTN, and SMX also showed substantial removals ranging between 50 % and 70 %. However, the remaining CECs presented modest removals (between 10 % and 35 %), except for ISTN, which did not show signs of degradation (<10 %).

The nature of the oxidants, when applied on an equimolar basis (1.2 mM of electrogenerated PMSA *vs.* 1.2 mM of commercial PDS), exerted the most significant influence on the degradation of BSPL, DRN, ISTN, and VLX in the RO_C treatment (t-student; p-value $\leq$ 0.01). Furthermore, this outcome was observed but to a lesser extent on the degradation of CBZ-EPX, LSTN, and SMX (t-student, p-value $\leq$ 0.05). The remaining CECs have not exhibited significant differences when applying electrogenerated PMSA or commercial PDS (p-value > 0.05) (Fig. 7a). Statistical analyses are detailed in Supplementary Material in Table SM-6 and SM-9.

Subsequently, similar photo-oxidation tests were conducted on the NF_C (*in situ* PMSA, test #3 and commercial PDS, test #4) under the same oxidant dosage (1.2 mM). Once more, the results indicated comparable levels of CECs degradation between the tests (Fig. 7b). For the 11 CECs present in the NF_C, there was an average decrease in concentration of 47 % for both tests #3 and #4. DCF and IOP were again the most easily degraded organic compounds, with removals exceeding 90 % and 80 %, respectively, followed by the antibiotic SMX and the herbicide DRN. The CBZ-EPX and LSTN contaminants had moderate degradations in both tests (~50 %), while BSPL and VLX showed low to moderate removals (between 20 % and 40 %). MLN was the only compound that showed resistance to photo-oxidation.

The impact of different oxidants on the phototreatment of CECs from NF_C was evaluated. Detailed statistical analyses can be found in Supplementary Material in Table SM-7, Table SM-8 and Table SM-9. When the same dose of oxidant was applied in the treatment of NF_C, only ISTN (Tukey's test; p-value $\leq$ 0.001) and SMX (Tukey's test; p-value $\leq$ 0.01) degradation processes were significantly affected by the nature of the oxidant (Fig. 7b). These findings suggest that the NF_C matrix is less sensitive to the oxidant type used than the RO_C treatment.

Given these results, some discussion on the mechanisms involved in the degradation of the CECs is required. In these photo-oxidation treatments, the breakdown of target molecules is driven by i) UVC photolysis, which depends on the ability of a target compound to absorb photons, influenced by the molar extinction coefficient (ε_{254nm}) and quantum yield (Φ_{254nm}), and ii) chemical oxidation by free radicals generated through photoactivation of the oxidizing agent. Therefore, compounds such as DCF, DRN, IOP, and SMX, with $\varepsilon_{254nm} \geq 10^3$ and/or $\Phi_{254nm} \geq 10^{-1}$ (Table SM-5), are more likely to absorb radiation and be degraded by photolysis than ATNL, CBZ, DEET, and VLX, presenting $\varepsilon_{254nm} \leq 10^2$ and/or $\Phi_{254nm} \leq 10^{-2}$. In the same rationale, CECs that have high kinetic reaction constants with free radicals ($k_{SO_4^{\bullet-}}$ and/or $k_{HO^{\bullet}} \geq 10^9$) will be more easily oxidized than those with lower k values, as is the case of MLN (Table SM-5).

The structural differences between PMS and PDS also lead to distinct preferential activation mechanisms to produce $SO_4^{\bullet-}$ radicals. Due to its asymmetric peroxide bond with a partial positive charge induced by the peroxide oxygen attached to hydrogen, transition metals activate PMS more efficiently [76]. In turn, PDS is preferentially active through energy transfer processes with a homolytic break of the peroxide bond due to its lower dissociation energy (92 kJ mol^{-1} compared to 377 kJ mol^{-1} for PMS) [76]. Associated with its greater susceptibility to UVC radiation, PDS is more readily activated by light at 254 nm ($\varepsilon_{S_2O_8^{2-}} = 21.1$ M^{-1} cm^{-1} *vs.* $\varepsilon_{HSO_5^-} = 14$ M^{-1} cm^{-1}) and has a higher quantum yield for radical production than PMS at ca. 250 nm ($\varphi_{SO_4^{\bullet-}} = 1.4$ for PDS *vs.* $\varphi_{SO_4^{\bullet-}} = 0.12$ and $\varphi_{SO_4^{\bullet-}} + {}_{HO^{\bullet}} = 1.04$ for PMS) [76,77]. From this perspective, it would be expected that the results obtained using commercial PDS would be superior to those achieved with electrochemically produced PMSA/PMS. However, it is essential to emphasize that the complexity of RO/NF matrices impacts the effectiveness of phototreatments. The presence of inorganic ions such as Cl^- and HCO_3^- can make PMS more effective than PDS in certain scenarios. Deng et al. [78] demonstrated that in treatments applying the UV/PS and UV/PMS processes, the addition of low concentrations of Cl^- resulted in a slight decrease in the degradation of CBZ. This effect can be attributed to the formation of $Cl^{\bullet}$ and $Cl_2^{\bullet-}$ radicals, which compete with $SO_4^{\bullet-}$ radicals. However, the addition of higher concentrations of Cl^- (> 1 mM) has a beneficial effect on the UV/PMS process, as the combination of PMS and Cl^- can generate active chlorine species such as HOCl and Cl_2 [78,79]. Regarding the presence of CO_3^{2-} and HCO_3^-, studies by Ao et al. [80] and Deng et al. [78] have shown that these ions inhibit the degradation of SMX and CBZ, respectively, in the UV/PS process. These inorganic species react with $SO_4^{\bullet-}$ radicals, producing less reactive radicals such as $CO_3^{\bullet-}$ and $HCO_3^{\bullet}$. In contrast, due to the asymmetric molecular structure of PMS, the presence of CO_3^{2-} and HCO_3^- ions in the matrices to be treated can beneficially activate PMS in UV/PMS reactions, leading to the production of more active species. Furthermore, the interaction of PMS with natural nucleophiles inherent in the matrices to be treated not only increases the production of $SO_4^{\bullet-}$ radicals but also facilitates the generation of other oxidant species that contribute to the oxidation of organic contaminants [76]. Moreover, the presence of dissolved or particulate organic also influences the efficiency of phototreatments by acting as a radical scavenger, reducing the availability of radicals to react with the CECs, and by blocking the transmission of UVC radiation, simultaneously affecting both the photolysis of the target compound and the generation of free radical species by photoactivation of the oxidant. A possible strategy to mitigate the scavenger effect of the dissolved and particulate organic matter is to replace the existing sand filter with a biofilter. This modification would enhance the control of the biodegradable organic content, thereby improving the overall efficiency of the treatment processes.

3.2.5. Optimizing treatment performance

The results from tests #1 to #4 underscore the efficacy of both *in situ* oxidant production (PMSA) and commercially acquired (PDS) in reducing the concentration of CECs in RO_C and NF_C. Despite variations in compound removal efficiencies, the overall trend suggests a significant decrease in contaminant levels, highlighting the potential of photo-oxidation as a viable treatment method. However, in pursuit of enhanced treatment performance and regulatory compliance, an additional test (#5) was conducted. This test involved doubling the dosage of the *in situ* produced oxidant (from 1.2 mM to 2.4 mM) and focusing on NF_C. The rationale behind this escalation was twofold: first, to assess whether increased oxidant concentration would yield higher removal efficiencies for CECs, particularly for compounds that exhibited moderate resistance in previous tests; second, to explore the possibility of achieving legal compliance for the COD parameter (not achieved in previous tests, see Table 3), a crucial aspect governed by environmental regulations.

The results of test #5 were promising, with an average decrease in concentrations for the 11 CECs present in the NF_C of 59 %, compared to

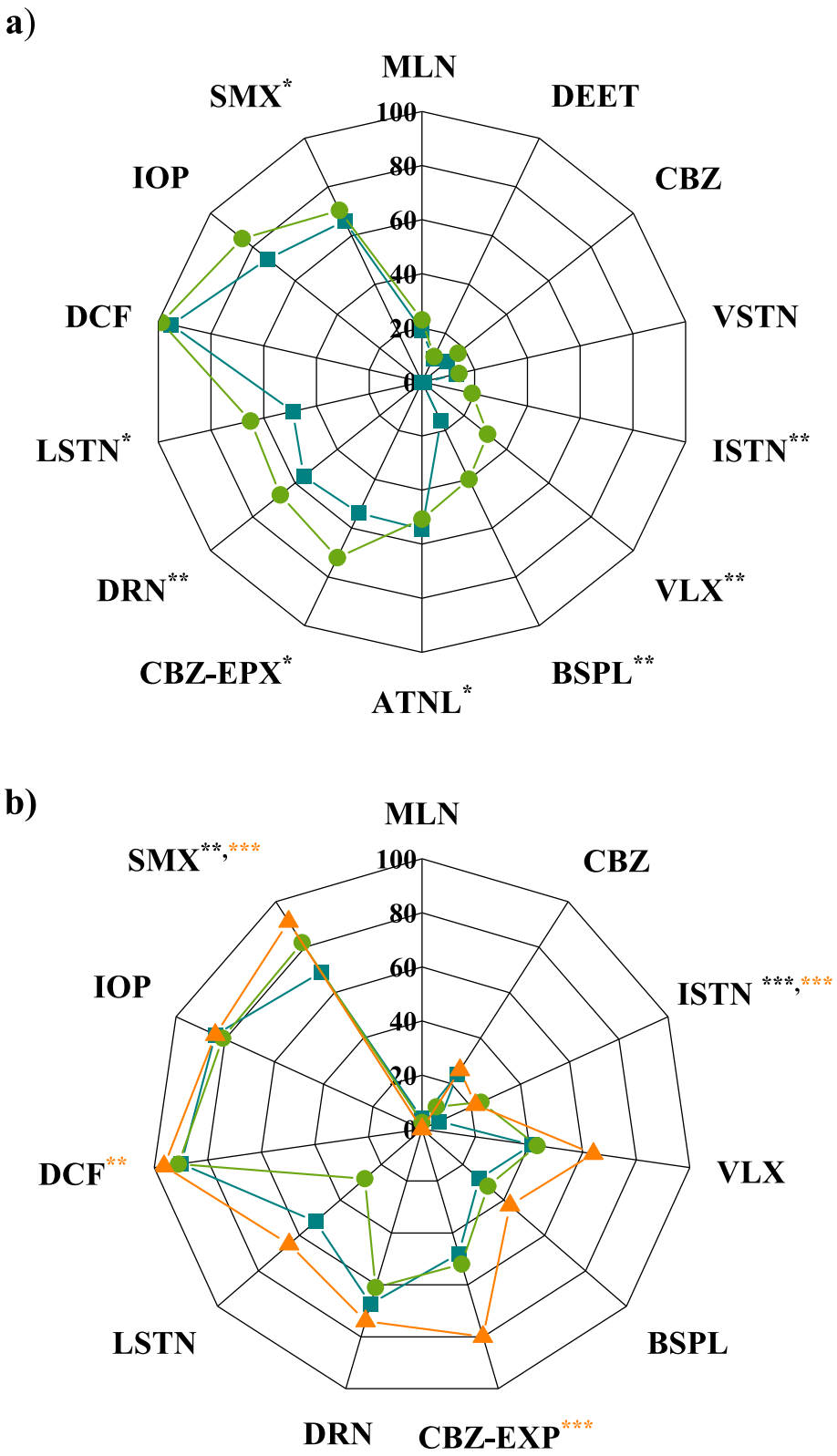

Fig. 7. Removal efficiencies (%) for the target CECs in a) RO_C (test #1, 1.2 mM PMSA; test #2, 1.2 mM PDS) and b) NF_C (test #3, 1.2 mM PMSA; test #4, 1.2 mM PDS and test #5, 2.4 mM PMSA). Differences between nature of oxidants are marked with asterisks (*** p-value ≤ 0.001; ** p-value ≤ 0.01; * p-value ≤ 0.05; 1.2 mM PMSA *vs*. 1.2 mM PDS, asterisks in black; 1.2 mM PMSA *vs*. 2.4 mM PMSA, asterisks in orange). Operational conditions: RT = 3.4 min; UVC radiation = 3.3 kJ/L. More operating conditions can be found in Table 3. Acronyms: ATNL – atenolol, BSPL – bisoprolol, CBZ – carbamazepine, CBZ-EPX – carbamazepine 10,11-epoxide, DCF diclofenac, IOP – iopromide, ISTN – irbesartan, LSTN – losartan, VSTN – valsartan, SMX – sulfamethoxazole, VLX – venlafaxine, DEET – N,N-diethyl-meta-toluamide, DRN – diuron, MLN – melamine. (For interpretation of the references to color in this figure legend, the reader is referred to the web version of this article.)

47 % in test #3, which had half the oxidant dosage (Fig. 7b). DCF was, once again, degraded at a concentration below the LQ (> 92 %), CBZ-EPX, IOP, and SMX were removed ≥80 %, and DRN, LSTN, and VLX also showed degradations between 65 % and 75 %. BSPL achieved ~40 % removal, while CBZ and ISTN did not go beyond 25 %. MLN showed no evidence of removal, again proving its resistance to photo-oxidation. Regarding statistical analysis, doubling the dose of electrogenerated PMSA (1.2 mM *vs.* 2.4 mM), the degradation of CBZ-EPX, ISTN, and SMX (Tukey's test; p-value $\leq$ 0.001) was the most significantly affected. It also significantly influenced the degradation of DCF (Tukey's test; p-value $\leq$ 0.01). Despite this, the removal efficiency of the other seven studied compounds was not affected (p-value > 0.05). This outcome suggests that although an increment on the removal of micropollutants was observed, increasing the PMSA dose have not impacted significantly. Nevertheless, applying 2.4 mM PMSA was crucial for meeting regulatory standards for COD in effluent discharge in agreement with Directive 91/271/EEC [68], with a final value of 116 mg L^{-1} (Table 3). In addition, at the end of the treatment, the TSS concentration was approximately equal to the initial concentration of this parameter in the untreated NF_C. Although this metric has not changed significantly, it also complies with Directive 91/271/EEC (<35 mg L^{-1}).

Nevertheless, further work is required to evaluate the i) stability of the electrodes used for oxidant generation, ii) stability of the ceramic membranes of the TMPr when using acidic oxidant solutions, and iii) mechanistic aspects of PMSA production and its decomposition kinetics at neutral pH. Moreover, scale-up of the system, as also LCA and LCC analysis, are important to increase the TRL of the technology.

4. Conclusions

The SERPIC-UCLM® cell demonstrated satisfactory mass transport rates, achieving k_mA values from (4.8 ± 0.1) × 10^{-3} s^{-1} to (11.76 ± 0.02) × 10^{-3} s^{-1} and *Sh* values from 343 ± 8 to 835 ± 2 for *Re* from 110 to 790. This cell outperformed some existing reactors reported in the literature as regards mass transport. The optimization of the initial pH of the electrolyte emerged as a critical factor for the successful integration of the SERPIC-UCLM® cell with the TMPr. The degradation tests were carried out in continuous mode operation, with a residence time of 3.4 min and a UV dose of 3.3 kJ L^{-1}. The continuous dosage of 1.2 mM electrogenerated PMSA (initial pH of the electrolyte of 1.0) and commercial PDS showed comparable degradation patterns for CECs in both RO_C and NF_C. Furthermore, doubling the oxidant dosage to 2.4 mM enhanced contaminant degradation efficiency and ensured compliance with regulatory standards regarding wastewater discharge into water bodies, particularly concerning pH, COD, and TSS levels. These findings highlight the potential of *in situ* electrochemical production of oxidants integrated with phototreatment processes, offering an innovative solution for improving wastewater treatment.

CRediT authorship contribution statement

Agustina R. de Olivera: Methodology, Investigation, Writing – original draft. **Carla S. Santos:** Methodology, Investigation, Writing – original draft. **Ismael F. Mena:** Methodology, Investigation, Writing – review & editing, Supervision, Validation. **Miguel A. Montiel:** Writing – review & editing, Validation, Supervision, Methodology. **Rosa Montes:** Writing – review & editing, Validation, Methodology, Investigation, Data curation. **José B. Quintana:** Writing – review & editing, Validation, Resources, Funding acquisition. **Rosario Rodil:** Writing – review & editing, Validation, Supervision, Resources, Methodology, Funding acquisition. **Ana I. Gomes:** Writing – review & editing, Supervision, Validation. **Francisca C. Moreira:** Writing – review & editing, Validation, Supervision. **Jan Gäbler:** Writing – review & editing, Project administration, Funding acquisition. **Lothar Schäfer:** Writing – review & editing, Project administration, Funding acquisition. **C. Sáez:** Writing – review & editing, Validation, Supervision, Resources, Project administration, Formal analysis. **Manuel A. Rodrigo:** Writing – review & editing, Resources, Project administration, Funding acquisition, Conceptualization. **Vítor J.P. Vilar:** Writing – review & editing, Resources, Project administration, Funding acquisition, Conceptualization.

Declaration of competing interest

The authors declare that they have no known competing financial interests or personal relationships that could have appeared to influence the work reported in this paper.

Acknowledgments

This work was financially supported by: (i) EU and Bundesministerium für Bildung und Forschung, Germany, Ministero dell'Università e della Ricerca, Italy, Agencia Estatal de Investigación, Spain, Fundação para a Ciência e a Tecnologia (FCT), Portugal, Norges forskningsråd, Norway, Water Research Commission, South Africa for funding, in the frame of the collaborative international consortium SERPIC financed under the ERA-NET AquaticPollutants Joint Transnational Call (GA N° 869178; Reference Aquatic/0002/2020 with DOI 10.54499/Aquatic/0002/2020). This ERA-NET is an integral part of the activities developed by the Water, Oceans and AMR Joint Programming Initiatives, (ii) national funds through FCT/MCTES (PIDDAC) – LSRE-LCM, UIDB/50020/2020 (DOI: 10.54499/UIDB/50020/2020) and UIDP/50020/2020 (DOI: 10.54499/UIDP/50020/2020), ALiCE, LA/P/0045/2020 (DOI: 10.54499/LA/P/0045/2020), (iii) Spanish Agencia Estatal de Investigación – MCIN/AEI/10.13039/501100011033 (ref. PID2020-117686RB-C32), and iv) regional funds Xunta de Galicia (ED431C 2021/06). Vítor J.P. Vilar and Francisca C. Moreira acknowledge the FCT Individual Call to Scientific Employment Stimulus 2017 (CEECIND/01317/2017 and CEECIND/02196/2017, respectively). Agustina R. de Olivera and Carla S. Santos acknowledge the PhD scholarships funded by FCT (2021.07416.BD and 2022.10796.BD, respectively).

Appendix A. Supplementary data

Supplementary data to this article can be found online at https://doi.org/10.1016/j.cej.2024.156900.

Data availability

Data will be made available on request.

References

[1] Water for sustainable food and agriculture water for sustainable food and agriculture: A report produced for the G20 presidency of Germany, Rome, 2017.
[2] L. Rizzo, S. Malato, D. Antakyali, V.G. Beretsou, M.B. Đolić, W. Gernjak, E. Heath, I. Ivancev-Tumbas, P. Karaolia, A.R. Lado Ribeiro, G. Mascolo, C.S. McArdell, H. Schaar, A.M.T. Silva, D. Fatta-Kassinos, Consolidated *vs.* new advanced treatment methods for the removal of contaminants of emerging concern from urban wastewater, Sci. Total Environ. 655 (2019) 986–1008, https://doi.org/10.1016/j.scitotenv.2018.11.265.
[3] A.I. Shah, M.U. Din Dar, R.A. Bhat, J.P. Singh, K. Singh, S.A. Bhat, Prospectives and challenges of wastewater treatment technologies to combat contaminants of emerging concerns, Ecol. Eng. 152 (2020) 105882, https://doi.org/10.1016/j.ecoleng.2020.105882.
[4] R.K. Mishra, S.S. Mentha, Y. Misra, N. Dwivedi, Emerging pollutants of severe environmental concern in water and wastewater: A comprehensive review on current developments and future research, Water-Energy Nexus. 6 (2023) 74–95, https://doi.org/10.1016/j.wen.2023.08.002.
[5] E. Parliament, Urban wastewater treatment, of 10 April 2024 on the proposal for a directive of the European Parliament and of the Council concerning urban wastewater treatment, 2024.
[6] A. Azaïs, J. Mendret, S. Gassara, E. Petit, A. Deratani, S. Brosillon, Nanofiltration for wastewater reuse: counteractive effects of fouling and matrice on the rejection of pharmaceutical active compounds, Sep. Purif. Technol. 133 (2014) 313–327, https://doi.org/10.1016/j.seppur.2014.07.007.
[7] J.C.G. Sousa, A.R. Ribeiro, M.O. Barbosa, M.F.R. Pereira, A.M.T. Silva, A review on environmental monitoring of water organic pollutants identified by EU guidelines,

J. Hazard. Mater. 344 (2018) 146–162, https://doi.org/10.1016/j.jhazmat.2017.09.058.
[8] D. Yadav, S. Rangabhashiyam, P. Verma, P. Singh, P. Devi, P. Kumar, C. Mustansar Hussain, G. Kumar Gaurav, K. Kumar Sathish, Environmental and health impacts of contaminants of emerging concerns : recent treatment challenges and approaches, Chemosphere 272 (2021), https://doi.org/10.1016/j.chemosphere.2020.129492, 129492.
[9] J.A. Khan, M. Sayed, S. Khan, N.S. Shah, D.D. Dionysiou, G. Boczkaj, Advanced oxidation processes for the treatment of contaminants of emerging concern, in: Contam. Emerg. Concern Water Wastewater Adv. Treat. Process., Elsevier Inc., 2020, pp. 299–365, https://doi.org/10.1016/B978-0-12-813561-7.00009-2.
[10] U. Hübner, S. Spahr, H. Lutze, A. Wieland, S. Rüting, W. Gernjak, J. Wenk, Advanced oxidation processes for water and wastewater treatment – guidance for systematic future research, Heliyon. 10 (2024) e30402, https://doi.org/10.1016/j.heliyon.2024.e30402.
[11] B. Cantoni, J. Ianes, B. Bertolo, S. Ziccardi, F. Maffini, M. Antonelli, Adsorption on activated carbon combined with ozonation for the removal of contaminants of emerging concern in drinking water, J. Environ. Manage. 350 (2024) 119537, https://doi.org/10.1016/j.jenvman.2023.119537.
[12] C.H. Chow, K.S.Y. Leung, Removing acesulfame with the peroxone process: Transformation products, pathways and toxicity, Chemosphere. 221 (2019) 647–655, https://doi.org/10.1016/j.chemosphere.2019.01.082.
[13] E. Asgari, A. Sheikhmohammadi, M. Mohammadian Fazli, R. Aali, F. Mohammadi, Comparative study on ozonation and catalytic ozonation using MgO@Fe_3O_4 magnetic nanoparticles for the removal of phenylamine from aqueous solutions, Int. J. Environ. Anal. Chem. (2022) 1–20, https://doi.org/10.1080/03067319.2022.2078198.
[14] G. Maniakova, I. Salmerón, M.I. Polo-López, I. Oller, L. Rizzo, S. Malato, Simultaneous removal of contaminants of emerging concern and pathogens from urban wastewater by homogeneous solar driven advanced oxidation processes, Sci. Total Environ. 766 (2021) 144320, https://doi.org/10.1016/j.scitotenv.2020.144320.
[15] F. Rodrigues-Silva, C.S. Santos, J.A. Marrero, R. Montes, J.B. Quintana, R. Rodil, O. C. Nunes, M.C.V.M. Starling, C.C. Amorim, A.I. Gomes, V.J.P. Vilar, Continuous UV-C/H_2O_2 and UV-C/Chlorine applied to municipal secondary effluent and nanofiltration retentate: Removal of contaminants of emerging concern, ecotoxicity, and reuse potential, Chemosphere. 361 (2024) 142355, https://doi.org/10.1016/j.chemosphere.2024.142355.
[16] L. Rizzo, T. Agovino, S. Nahim-Granados, M. Castro-Alférez, P. Fernández-Ibáñez, M.I. Polo-López, Tertiary treatment of urban wastewater by solar and UV-C driven advanced oxidation with peracetic acid: effect on contaminants of emerging concern and antibiotic resistance, Water Res. 149 (2019) 272–281, https://doi.org/10.1016/j.watres.2018.11.031.
[17] A. Sheikhmohammadi, E. Asgari, N. Alinejad, B. Hashemzadeh, Photocatalytic oxidation of ciprofloxacin by UV/ α-Fe_2O_3/sulfite: mechanism, kinetic, degradation pathway, Int. J. Environ. Health Res. 33 (2023) 192–205, https://doi.org/10.1080/09603123.2021.2013453.
[18] J.Q. Chen, G.N. Zhou, R.R. Ding, Q. Li, H.Q. Zhao, Y. Mu, Ferrous ion enhanced Fenton-like degradation of emerging contaminants by sulfidated nanosized zero-valent iron with pH insensitivity, J. Hazard. Mater. 459 (2023) 132229, https://doi.org/10.1016/j.jhazmat.2023.132229.
[19] A. Sheikhmohammadi, H. Alamgholiloo, M. Golaki, P. Khakzad, E. Asgari, F. Rahimlu, Cefixime removal via WO_3/Co-ZIF nanocomposite using machine learning methods, Sci. Rep. 14 (2024) 13840, https://doi.org/10.1038/s41598-024-64790-2.
[20] N. Nippatlapalli, A. Ganta, Recent progress on application of nonthermal plasma for the degradation of aqueous emerging contaminants: A review on mechanism, reactor strategies, integrated systems and future perspective, Process Saf. Environ. Prot. 187 (2024) 1454–1470, https://doi.org/10.1016/j.psep.2024.05.009.
[21] F.C. Moreira, R.A.R. Boaventura, E. Brillas, V.J.P. Vilar, Electrochemical advanced oxidation processes: A review on their application to synthetic and real wastewaters, Appl. Catal. B Environ. 202 (2017) 217–261, https://doi.org/10.1016/j.apcatb.2016.08.037.
[22] S. Giannakis, K.Y.A. Lin, F. Ghanbari, A review of the recent advances on the treatment of industrial wastewaters by sulfate radical-based advanced oxidation processes (SR-AOPs), Chem. Eng. J. 406 (2021) 127083, https://doi.org/10.1016/j.cej.2020.127083.
[23] E.T. Yun, H.Y. Yoo, H. Bae, H. Il Kim, J. Lee, Exploring the role of persulfate in the activation process: Radical precursor versus electron acceptor, Environ. Sci. Technol. 51 (2017) 10090–10099, https://doi.org/10.1021/acs.est.7b02519.
[24] B. Li, Y.F. Wang, L. Zhang, H.Y. Xu, Enhancement strategies for efficient activation of persulfate by heterogeneous cobalt-containing catalysts: a review, Chemosphere. 291 (2022) 132954, https://doi.org/10.1016/j.chemosphere.2021.132954.
[25] D.T. Oyekunle, E.A. Gendy, J. Ifthikar, Z. Chen, Heterogeneous activation of persulfate by metal and non-metal catalyst for the degradation of sulfamethoxazole: a review, Chem. Eng. J. 437 (2022) 135277, https://doi.org/10.1016/j.cej.2022.135277.
[26] J. Yang, M. Zhu, D.D. Dionysiou, What is the role of light in persulfate-based advanced oxidation for water treatment? Water Res. 189 (2021) 116627 https://doi.org/10.1016/j.watres.2020.116627.
[27] S. He, Y. Chen, X. Li, L. Zeng, M. Zhu, Heterogeneous photocatalytic activation of persulfate for the removal of organic contaminants in water: a critical review, ACS ES&T Eng. 2 (2022) 527–546, https://doi.org/10.1021/acsestengg.1c00330.
[28] S. Guerra-Rodríguez, M.J. Abeledo-Lameiro, M.I. Polo-López, P. Plaza-Bolaños, A. Agüera, E. Rodríguez, J. Rodríguez-Chueca, Pilot-scale sulfate radical-based advanced oxidation for wastewater reuse: simultaneous disinfection, removal of contaminants of emerging concern, and antibiotic resistance genes, Chem. Eng. J. 477 (2023) 146916, https://doi.org/10.1016/j.cej.2023.146916.
[29] I. Berruti, S. Nahim-granados, I. Oller, UV-C peroxymonosulfate activation for wastewater regeneration: simultaneous inactivation of pathogens and degradation of contaminants of emerging concern, Molecules. 26 (2021) 4890, https://doi.org/10.3390/molecules26164890.
[30] C. Drossou, Y. Petrakis, K. Tyrovola, N.P. Xekoukoulotakis, Photochemical degradation of the antidepressant sertraline in aqueous solutions by UVC, UVC/H_2O_2, and UVC/$S_2O_8^{2-}$, Water Res. 217 (2022) 118442 https://doi.org/10.1016/j.watres.2022.118442.
[31] L. Sbardella, I.V. Gala, J. Comas, S.M. Carbonell, I. Rodríguez-Roda, W. Gernjak, Integrated assessment of sulfate-based AOPs for pharmaceutical active compound removal from wastewater, J. Clean. Prod. 260 (2020) 121014, https://doi.org/10.1016/j.jclepro.2020.121014.
[32] J. Gao, C. Luo, L. Gan, D. Wu, F. Tan, X. Cheng, W. Zhou, S. Wang, F. Zhang, J. Ma, A comparative study of UV/H_2O_2 and UV/PDS for the degradation of micro-pollutants: Kinetics and effect of water matrix, Environ. Sci. Pollut. Res. 27 (2020) 24531–24541, https://doi.org/10.1007/s11356-020-08794-1.
[33] M. Nihemaiti, D.B. Miklos, U. Hübner, K.G. Linden, J.E. Drewes, J.P. Croué, Removal of trace organic chemicals in wastewater effluent by UV/H_2O_2 and UV/PDS, Water Res. 145 (2018) 487–497, https://doi.org/10.1016/j.watres.2018.08.052.
[34] A.V. Karim, Y. Jiao, M. Zhou, P.V. Nidheesh, Iron-based persulfate activation process for environmental decontamination in water and soil, Chemosphere. 265 (2021) 129057, https://doi.org/10.1016/j.chemosphere.2020.129057.
[35] L. Vazquez, L.M.M.T. Gomes, P.H. Presumido, D.G.D. Rocca, R.F.P.M. Moreira, T. Dagnac, M. Llompart, A.I. Gomes, V.J.P. Vilar, Tubular membrane photoreactor for the tertiary treatment of urban wastewater towards antibiotics removal: Application of different photocatalyst / oxidant combinations and ozonation, J. Environ. Chem. Eng. 11 (2023) 109766, https://doi.org/10.1016/j.jece.2023.109766.
[36] M.P. Castro, I.F. Mena, M.A. Montiel, J. Gäbler, L. Schäfer, C. Sáez, M.A. Rodrigo, Optimization of the electrolytic production of Caro's acid. Towards industrial production using diamond electrodes, Sep. Purif. Technol. 320 (2023) 124118, https://doi.org/10.1016/j.seppur.2023.124118.
[37] M.P. Castro, M.A. Montiel, I.F. Mena, J. Gäbler, H. King, C. Sáez, M.A. Rodrigo, Outstanding productions of peroxymonosulfuric acid combining tailored electrode coating and 3D printing, J. Water Process Eng. 53 (2023) 103902, https://doi.org/10.1016/j.jwpe.2023.103902.
[38] S.A. Bueno, G. de Oliveira Santiago Santos, T. Oliveira Silva, M.R. Vasconcelos Lanza, P. Balderas Hernández, G. Roa Morales, J. Ibáñez Cornejo, C. Sáez, M.A. Rodrigo, Sustainable integrated process for cogeneration of oxidants for VOCs removal, Chemosphere. 342 (2023) 140171, https://doi.org/10.1016/j.chemosphere.2023.140171.
[39] S.Q. Yang, Y.H. Cui, Y.Y. Liu, Z.Q. Liu, X.Y. Li, Electrochemical generation of persulfate and its performance on 4-bromophenol treatment, Sep. Purif. Technol. 207 (2018) 461–469, https://doi.org/10.1016/j.seppur.2018.06.071.
[40] K. Serrano, P.A. Michaud, C. Comninellis, A. Savall, Electrochemical preparation of peroxodisulfuric acid using boron doped diamond thin film electrodes, Electrochim. Acta. 48 (2002) 431–436, https://doi.org/10.1016/S0013-4686(02)00688-6.
[41] J. Zhu, K.K. Hii, K. Hellgardt, Toward a green generation of oxidant on demand: Practical electrosynthesis of ammonium persulfate, ACS Sustain. Chem. Eng. 4 (2016) 2027–2036, https://doi.org/10.1021/acssuschemeng.5b01372.
[42] H. Luo, C. Li, X. Sun, B. Bin Ding, Cathodic indirect oxidation of organic pollutant paired to anodic persulfate production, J. Electroanal. Chem. 792 (2017) 110–116, https://doi.org/10.1016/j.jelechem.2017.03.040.
[43] J. Liu, S. Zhong, Y. Song, B. Wang, F. Zhang, Degradation of tetracycline hydrochloride by electro-activated persulfate oxidation, J. Electroanal. Chem. 809 (2018) 74–79, https://doi.org/10.1016/j.jelechem.2017.12.033.
[44] D.L. Ball, J.O. Edwards, The kinetics and mechanism of the decomposition of Caro's Acid. I, J. Am. Chem. Soc. 78 (1956) 1125–1129, https://doi.org/10.1021/ja01587a011.
[45] V.J.P. Vilar, P. Alfonso-Muniozguren, J.P. Monteiro, J. Lee, S.M. Miranda, R.A. R. Boaventura, Tube-in-tube membrane microreactor for photochemical UVC/H_2O_2 processes: A proof of concept, Chem. Eng. J. 379 (2020) 122341, https://doi.org/10.1016/j.cej.2019.122341.
[46] E. Lumbaque Cuervo, D.S. Lüdtke, D.D. Dionysiou, V.J.P. Vilar, C. Sirtori, Tube-in-tube membrane photoreactor as a new technology to boost sulfate radic al advanced oxidation processes, Water Res. 191 (2021) 116815, https://doi.org/10.1016/j.watres.2021.116815.
[47] C. Santos, M. Herraiz-Carboné, E. Lacasa, C. Sáez, R. Montes, J.B. Quintana, R. Rodil, A.I. Gomes, V.J.P. Vilar, Continuous-flow titration of low iron doses to promote photo-Fenton and photo-Fenton-like processes at neutral pH, Chem. Eng. J. 476 (2023) 146655, https://doi.org/10.1016/j.cej.2023.146655.
[48] R.M. Castellanos, J. Paulo Bassin, M. Dezotti, R.A.R. Boaventura, V.J.P. Vilar, Tube-in-tube membrane reactor for heterogeneous TiO_2 photocatalysis with radial addition of H_2O_2, Chem. Eng. J. 395 (2020) 124998, https://doi.org/10.1016/j.cej.2020.124998.
[49] P. Verlicchi, V. Grillini, E. Lacasa, E. Archer, P. Krzeminski, A.I. Gomes, V.J. P. Vilar, M.A. Rodrigo, J. Gäbler, L. Schäfer, Selection of indicator contaminants of emerging concern when reusing reclaimed water for irrigation — a proposed methodology, Sci. Total Environ. 873 (2023) 162359, https://doi.org/10.1016/j.scitotenv.2023.162359.
[50] P. Verlicchi, E. Lacasa, V. Grillini, Quantitative and qualitative approaches for CEC prioritization when reusing reclaimed water for irrigation needs – a critical review,

Sci. Total Environ. 900 (2023) 165735, https://doi.org/10.1016/j.scitotenv.2023.165735.
[51] D.R. Lide, Handbook of Chemistry and Physics, 84th ed., CRC Press, Boca Raton, 2004.
[52] J.R. Selman, C.W. Tobias, Mass-Transfer Measurements by the Limiting-Current Technique, Academic Press, Cambridge, 1978.
[53] J. Hereijgers, J. Schalck, T. Breugelmans, Mass transfer and hydrodynamic characterization of structured 3D electrodes for electrochemistry, Chem. Eng. J. 384 (2020) 123283, https://doi.org/10.1016/j.cej.2019.123283.
[54] L.F. Arenas, C. Ponce de León, F.C. Walsh, 3D-printed porous electrodes for advanced electrochemical flow reactors: a Ni/stainless steel electrode and its mass transport characteristics, Electrochem. Commun. 77 (2017) 133–137, https://doi.org/10.1016/j.elecom.2017.03.009.
[55] L. Vázquez, A. Alvarez-Gallegos, F.Z. Sierra, C.P. de León, F.C. Walsh, Prediction of mass transport profiles in a laboratory filter-press electrolyser by computational fluid dynamics modelling, Electrochim. Acta. 55 (2010) 3446–3453, https://doi.org/10.1016/j.electacta.2009.08.067.
[56] P. Cañizares, J. García-Gómez, I. Fernández de Marcos, M.A. Rodrigo, J. Lobato, Measurement of mass-transfer coefficients by an electrochemical technique, J. Chem. Educ. 83 (2006) 1204–1207, https://doi.org/10.1021/ed083p1204.
[57] M. Griffiths, C.P. De León, F.C. Walsh, Mass transport in the rectangular channel of a filter-press electrolyzer (the FM01-LC reactor), AIChE J. 51 (2005) 682–687, https://doi.org/10.1002/aic.10311.
[58] R.B. Bird, W.E. Stewart, E.N. Lightfoot, Transport Phenomena, 2nd ed., John Wiley & Sons, New Jersey, 2001, p. 2001.
[59] F.C. Walsh, A First Course in Electrochemical Engineering, 4th ed., Electrochemical Consultancy, Hants England, 1993.
[60] F.J. Recio, P. Herrasti, L. Vazquez, C. Ponce De León, F.C. Walsh, Mass transfer to a nanostructured nickel electrodeposit of high surface area in a rectangular flow channel, Electrochim. Acta. 90 (2013) 507–513, https://doi.org/10.1016/j.electacta.2012.11.135.
[61] L.F. Arenas, C.P. de León, F.C. Walsh, Mass transport and active area of porous Pt/Ti electrodes for the Zn-Ce redox flow battery determined from limiting current measurements, Electrochim. Acta. 221 (2016) 154–166, https://doi.org/10.1016/j.electacta.2016.10.097.
[62] S. Langlois, F. Coeuret, Flow-through and flow-by porous electrodes of nickel foam. II. Diffusion-convective mass transfer between the electrolyte and the foam, J. Appl. Electrochem. 19 (1989) 51–60, https://doi.org/10.1007/BF01039389.
[63] A. Abahussain, C. Ponce de Leon, F.C. Walsh, Mass-transfer measurements at porous 3D Pt-Ir/Ti electrodes in a direct borohydride fuel cell, J. Electrochem. Soc. 165 (2018) F198–F206, https://doi.org/10.1149/2.0751803jes.
[64] D.F.S. Morais, B. Lopes, M.M. Dias, V.J.P. Vilar, F.C. Moreira, e^- NETmix: A pioneering electrochemical flow reactor with enhanced mass transfer, Chem. Eng. J. 481 (2024) 148244, https://doi.org/10.1016/j.cej.2023.148244.
[65] J.L.C. Santos, V. Geraldes, S. Velizarov, J.G. Crespo, Characterization of fluid dynamics and mass-transfer in an electrochemical oxidation cell by experimental and CFD studies, Chem. Eng. J. 157 (2010) 379–392, https://doi.org/10.1016/j.cej.2009.11.021.
[66] E.P. Rivero, F.F. Rivera, M.R. Cruz-Díaz, E. Mayen, I. González, Numerical simulation of mass transport in a filter press type electrochemical reactor FM01-LC: Comparison of predicted and experimental mass transfer coefficient, Chem. Eng. Res. Des. 90 (2012) 1969–1978, https://doi.org/10.1016/j.cherd.2012.04.010.
[67] R.A. Márquez-Montes, V.H. Collins-Martínez, I. Pérez-Reyes, D. Chávez-Flores, O. A. Graeve, V.H. Ramos-Sánchez, Electrochemical engineering assessment of a novel 3D-printed filter-press electrochemical reactor for multipurpose laboratory applications, ACS Sustain. Chem. Eng. 8 (2020) 3896–3905, https://doi.org/10.1021/acssuschemeng.9b07368.
[68] E. (ed). Council, Council Directive 91/271/EEC of 21st of May 1991 concerning urban wastewater treatment, 1991.
[69] A. Schranck, K. Doudrick, Effect of reactor configuration on the kinetics and nitrogen byproduct selectivity of urea electrolysis using a boron doped diamond electrode, Water Res. 168 (2020) 115130, https://doi.org/10.1016/j.watres.2019.115130.
[70] A.V. Martins Almeida, Degradação de Poluentes Emergentes em Águas Através de Processos Integrados com ozono, Master Thesis, Faculty of Engineering, University of Porto, Porto, 2017.
[71] Z.U.H. Khan, N.S. Gul, S. Sabahat, J. Sun, K. Tahir, N.S. Shah, N. Muhammad, A. Rahim, M. Imran, J. Iqbal, T.M. Khan, S. Khasim, U. Farooq, J. Wu, Removal of organic pollutants through hydroxyl radical-based advanced oxidation processes, Ecotoxicol. Environ. Saf. 267 (2023) 115564, https://doi.org/10.1016/j.ecoenv.2023.115564.
[72] A. Yusuf, A. Giwa, J.O. Eniola, H.K. Amusa, M.R. Bilad, Recent advances in catalytic sulfate radical-based approach for removal of emerging contaminants, J. Hazard. Mater. Adv. 7 (2022) 100108, https://doi.org/10.1016/j.hazadv.2022.100108.
[73] A.R. Lado Ribeiro, N.F.F. Moreira, G. Li Puma, A.M.T. Silva, Impact of water matrix on the removal of micropollutants by advanced oxidation technologies, Chem. Eng. J. 363 (2019) 155–173, https://doi.org/10.1016/j.cej.2019.01.080.
[74] L. Lian, B. Yao, S. Hou, J. Fang, S. Yan, W. Song, Kinetic study of hydroxyl and sulfate radical-mediated oxidation of pharmaceuticals in wastewater effluents, Environ. Sci. Technol. 51 (2017) 2954–2962, https://doi.org/10.1021/acs.est.6b05536.
[75] D. Zhou, H. Zhang, L. Chen, Sulfur-replaced Fenton systems: can sulfate radical substitute hydroxyl radical for advanced oxidation technologies? J. Chem. Technol. Biotechnol. 90 (2015) 775–779, https://doi.org/10.1002/jctb.4525.
[76] J. Lee, U. Von Gunten, J. Kim, Persulfate-based advanced oxidation: critical assessment of opportunities and roadblocks, Environ. Sci. Technol. 54 (2020) 3064–3081, https://doi.org/10.1021/acs.est.9b07082.
[77] C. Luo, J. Ma, J. Jiang, Y. Liu, Y. Song, Y. Yang, Y. Guan, D. Wu, Simulation and comparative study on the oxidation kinetics of atrazine by UV/H_2O_2, UV/HSO_5^- and UV/$S_2O_8^{2-}$, Water Res. 80 (2015) 99–108, https://doi.org/10.1016/j.watres.2015.05.019.
[78] J. Deng, Y. Shao, N. Gao, S. Xia, C. Tan, S. Zhou, X. Hu, Degradation of the antiepileptic drug carbamazepine upon different UV-based advanced oxidation processes in water, Chem. Eng. J. 222 (2013) 150–158, https://doi.org/10.1016/j.cej.2013.02.045.
[79] R. Yuan, S.N. Ramjaun, Z. Wang, J. Liu, Effects of chloride ion on degradation of Acid Orange 7 by sulfate radical-based advanced oxidation process: implications for formation of chlorinated aromatic compounds, J. Hazard. Mater. 196 (2011) 173–179, https://doi.org/10.1016/j.jhazmat.2011.09.007.
[80] X. Ao, W. Liu, Degradation of sulfamethoxazole by medium pressure UV and oxidants: peroxymonosulfate, persulfate, and hydrogen peroxide, Chem. Eng. J. 313 (2017) 629–637, https://doi.org/10.1016/j.cej.2016.12.089.
[81] C.J. Brown, D. Pletcher, F.C. Walsh, J.K. Hammond, D. Robinson, Studies of space-averaged mass transport in the FM01-LC laboratory electrolyser, J. Appl. Electrochem. 23 (1993) 38–43, https://doi.org/10.1007/BF00241573.
[82] T.R. Ralph, M.L. Hitchman, J.P. Millington, F.C. Walsh, Mass transport in an electrochemical laboratory filterpress reactor and its enhancement by turbulence promoters, Electrochim. Acta. 41 (1996) 591–603.
[83] L.S. Clesceri, A.E. Greenberg, R.R. Trussell, Standard Methods for the Examination of Water and Wastewater, 23rd ed., American Public Health Association, American Water Works Association, Water Environment Federation, Washington DC, 2017.